REPORT DOCUMENTATION PAGE

Form Approved
OMB No. 0704-0188

1. AGENCY USE ONLY *(Leave blank)*	2. REPORT DATE	3. REPORT TYPE AND DATES COVERED
	April 30, 1996	April 1, 1995 to March 31, 1996 FINAL

4. TITLE AND SUBTITLE
Influence of Surface Roughness on Guided Waves in Plates

5. FUNDING NUMBERS
F49620-95-1-0294

6. AUTHORS
Dale E. Chimenti and Oleg I. Lobkis

7. PERFORMING ORGANIZATION NAME(S) AND ADDRESS(ES)
Iowa State University
Center for NDE
125 ASC-II
Ames, IA 50011

AFOSR-TR-96
0448

9. SPONSORING/MONITORING AGENCY NAME(S) AND ADDRESS(ES)
Air Force office of Scientific Research
Aerospace Directorate
Bolling Air Force Base, Washington, DC
NA

10. SPONSORING/MONITORING AGENCY REPORT NUMBER
F49620-95-1-0294

11. SUPPLEMENTARY NOTES

12a. DISTRIBUTION/AVAILABILITY STATEMENT
APPROVED FOR PUBLIC RELEASE; DISTRIBUTION IS UNLIMITED

12b. DISTRIBUTION CODE

13. ABSTRACT *(Maximum 200 words)*

This report covers fundamental research performed on the effect of surface roughness on ultrasonic guided waves in plates. The effort reported here consists both of experiments and calculations. The measurements exploit guided waves generated in either immersion or with contact coupling. Samples have included aluminum prepared by indenting or sandblasting. The sandblasted specimens have been Independently profiled to determine rms roughness. A simple model calculation is also described which, using analytical methods only, has led to a successful approximate theoretical description of guided wave attenuation caused by scattering from randomly rough surfaces. The model takes advantage of the Kirchhoff approximation, in which the rough surface wave interaction is assumed to be restricted to the signal phase. This phase-screen method is applied to guided plate waves through Auld's transverse-resonance approach to derive a dispersion relation of the rough waveguide. This calculation is generalized to fluid-immersed plates having only a single rough surface either on the same or opposite side of the plate as the ultrasonic transducers. Detailed comparisons between the results of the experimental study and predictions of the model calculations show good agreement, generally demonstrating the utility of the theoretical approach over a reasonably wide range of variation of the experimental parameters.

14. SUBJECT TERMS Guided elastic waves, Plates, Surface roughness, Corrosion, Immersion coupling, Contact coupling, Knife-edge, Aluminum alloys, Sandblasted, Indented, Kirchhoff model, phase-screen approximation, transverse-resonance, Partial waves, Experiments, Model predictions

15. NUMBER OF PAGES
57

16. PRICE CODE

17. SECURITY CLASSIFICATION OF REPORT	18. SECURITY CLASSIFICATION OF THIS PAGE	19. SECURITY CLASSIFICATION OF ABSTRACT	20. LIMITATION OF ABSTRACT
UNLIMITED	UNLIMITED	UNLIMITED	U

Abstract

This report covers fundamental research performed on the effect of surface roughness on ultrasonic guided waves in plates. The effort reported here consists both of experiments and calculations. The measurements exploit guided waves generated in either immersion or with contact coupling. Samples have included aluminum prepared by indenting or sandblasting. The sandblasted specimens have been independently profiled to determine rms roughness. A simple model calculation is also described which, using analytical methods only, has led to a successful approximate theoretical description of guided wave attenuation caused by scattering from randomly rough surfaces. The model takes advantage of the Kirchhoff approximation, in which the rough surface wave interaction is assumed to be restricted to the signal phase. This phase-screen method is applied to guided plate waves through Auld's transverse-resonance approach to derive a dispersion relation of the rough waveguide. This calculation is generalized to fluid-immersed plates having only a single rough surface either on the same or opposite side of the plate as the ultrasonic transducers. Detailed comparisons between the results of the experimental study and predictions of the model calculations show good agreement, generally demonstrating the utility of the theoretical approach over a reasonably wide range of variation of the experimental parameters.

Contents

Acknowledgments vi

Executive Summary vii

1 Background 1

2 Theoretical Development 3

2.1 RS Waveguide Dispersion Relation 3

2.2 Generalized Scattering Coefficients for RS Plate 8

3 Experimental Technique 17

4 Results and Discussion 21

4.1 Immersion Experiments 22

4.2 Contact Measurements 41

4.3 Knife-Edge Contact Coupling 48

5 Summary and Recommendations 53

References 55

List of Figures

1 Pole trajectories in the complex plane for three antisymmetric plate modes, showing strong dependence of damping part on incident angle. Inset shows experimental geometry and defines axes. 6

2 Reflection series for an internally incident s and p wave in a plate. In b) wave leakage is illustrated at the upper plate surface. 10

3 Plane wave reflection coefficient magnitude for progressively increasing roughness on the upper plate surface (facing transducers); rms roughness $h = 0$ (solid curve), $h = 30$ μm (dashed), and $h = 100$ μm (dotted). Plate thickness is 1.37 mm and incident angle is 20°. 12

4 Plane wave reflection coefficient magnitude for progressively increasing roughness on the lower plate surface (away from transducers); rms roughness $h = 0$ (solid curve), $h = 30$ μm (dashed), and $h = 100$ μm (dotted). Plate thickness is 1.37 mm and incident angle is 20°. 13

5 Plane wave reflection coefficient magnitude for progressively increasing roughness on the lower plate surface (away from incident wave); rms roughness $h = 0$ (solid curve), $h = 30$ μm (dashed), and $h = 100$ μm (dotted). Plate thickness is 1.37 mm and fixed frequency is 8 MHz. 15

6 Plane wave reflection coefficient magnitude for progressively increasing roughness on the upper plate surface (towards incident wave); rms roughness $h = 0$ (solid curve), $h = 15$ μm (dashed), and $h = 30$ μm (dotted). Plate thickness is 1.37 mm and fixed frequency is 8 MHz. 16

7 Block diagram of experimental apparatus, showing signal generation and detection channels. 18

8 Schematic diagram of immersion experiments showing the deployment of the transducers and the parameters varied. 19

9 Schematic diagram of contact experiments showing the deployment of the transducers and the parameters varied. 20

10 Theoretical and experimental frequency dependence of receiver voltage for smooth (solid) and lower rough surfaces with $h = 13$ μm (dashed) and $h = 26$ μm (dotted), with x_i=-10 mm, and incidence at 20°. 23

11 Theoretical and experimental frequency dependence of receiver voltage for smooth (solid) and lower rough surfaces with $h = 13$ μm (dashed) and $h = 26$ μm (dotted), with $x_i = 0$ mm, and incidence at 20°. 24

12 Theoretical and experimental frequency dependence of receiver voltage for smooth (solid) and lower rough surfaces with $h = 13$ μm (dashed) and $h = 26$ μm (dotted), with $x_i = 5$ mm, and incidence at 20°. 26

13 Theoretical and experimental frequency dependence of receiver voltage for smooth (solid) and lower rough surfaces with $h = 13$ μm (dashed) and $h = 26$ μm (dotted), with $x_i = 10$ mm, and incidence at 20°. 27

14 Theoretical and experimental frequency dependence of receiver voltage for smooth (solid) and lower rough surfaces with $h = 13$ μm (dashed) and $h = 26$ μm (dotted), with $x_i = 20$ mm, and incidence at 20°. 28

15 Theoretical and experimental frequency dependence of receiver voltage for smooth (solid) and lower rough surfaces with $h = 13$ μm (dashed) and $h = 26$ μm (dotted), with $x_i = 30$ mm, and incidence at 20°. 29

16 Theoretical and experimental frequency dependence of receiver voltage for smooth (solid) and upper rough surfaces with $h = 13$ μm (dashed) and $h = 26$ μm (dotted), with $x_i = 0$ mm, and incidence at 20°. 31

17 Theoretical and experimental frequency dependence of receiver voltage for smooth (solid) and upper rough surfaces with $h = 13$ μm (dashed) and $h = 26$ μm (dotted), with $x_i = 10$ mm, and incidence at 20°. 32

18 Theoretical and experimental frequency dependence of receiver voltage for smooth (solid) and lower rough surfaces with $h = 13$ μm (dashed) and $h = 26$ μm (dotted), with $x_i = 0$ mm, and incidence at 10°. 33

19 Theoretical and experimental frequency dependence of receiver voltage for smooth (solid) and lower rough surfaces with $h = 13$ μm (dashed) and $h = 26$ μm (dotted), with $x_i = 10$ mm, and incidence at 10°. 34

20 Theoretical and experimental frequency dependence of receiver voltage for smooth (solid) and lower rough surfaces with $h = 13$ μm (dashed) and $h = 26$ μm (dotted), with $x_i = 30$ mm, and incidence at 10°. 35

21 Theoretical and experimental frequency dependence of receiver voltage for smooth (solid) and upper rough surfaces with $h = 13$ μm (dashed) and $h = 26$ μm (dotted), with $x_i = 0$ mm, and incidence at 10°. 37

22 Theoretical and experimental frequency dependence of receiver voltage for smooth (solid) and upper rough surfaces with $h = 13$ μm (dashed) and $h = 26$ μm (dotted), with $x_i = 10$ mm, and incidence at 10°. 38

23 Theoretical and experimental frequency dependence of receiver voltage for smooth (solid) and upper rough surfaces with $h = 13$ μm (dashed) and $h = 26$ μm (dotted), with $x_i = 30$ mm, and incidence at 10°. 39

24 Theoretical and experimental dependence on displacement x_i of receiver voltage for smooth (solid) and lower rough surfaces with $h = 13$ μm (dashed) and $h = 26$ μm (dotted) and incidence at 20° for the S_5 mode at 11 MHz. 40

25 Theoretical and experimental dependence on displacement x_i of receiver voltage for smooth (solid) and lower rough surfaces with $h = 13$ μm (dashed) and $h = 26$ μm (dotted) and incidence at 10° for the S_3 mode at 3.22 MHz. 42

26 Theoretical and experimental dependence on displacement x_i of receiver voltage for smooth (solid) and lower rough surfaces with $h = 13$ μm (dashed) and $h = 26$ μm (dotted) and incidence at 10° for the S_7 mode at 7.75 MHz. 43

27 Shoe-contact experimental signal from rough aluminum sandblasted plates ($h = 26$ μm) for three different transducer axis separations x_i (solid: 20 mm; dashed: 30 mm; dotted: 40 mm); top frame is thin plate (1.4 mm) and bottom frame is thick plate (2.3 mm). 45

28 Collected experimental data for rough aluminum plates as a function of transducer axis separations x_i; three modes are illustrated for each of the two rms roughnesses, $h = 13$ μm and $h = 26$ μm. 46

29 Shoe-contact experimental signal from rough aluminum plates ($h = 44$ μm) for two different roughness lengths L (solid: no roughness; dashed: 12.7 mm roughness section; dotted: 25.4 mm). Inset shows roughness on same side as transducers. 47

30 Shoe-contact experimental signal from rough aluminum plates ($h = 60$ μm) for four different roughness lengths L (solid: no roughness; dashed: 12.7 mm roughness section; dotted: 25.4 mm; chain dot: 38.1 mm; solid: 50.8 mm). Inset shows roughness on same side as transducers. 49

31 Shoe-contact experimental signal from rough aluminum plates ($h = 60$ μm) for four different roughness lengths L (solid: no roughness; dashed: 12.7 mm roughness section; dotted: 25.4 mm; chain dot: 38.1 mm; solid: 50.8 mm). Inset shows roughness on opposite side as transducers. 50

32 Collected experimental data for rough aluminum plates as a function of roughness section length L; two modes are illustrated for the 60-μmrms roughness plate, S_1 and A_1. 51

33 Knife-edge contact experimental signals from rough aluminum plates (dashed: $h = 13$ μm; dotted: $h = 26$ μm) for a transducer separation $x_i = 22$ mm. Sharp decrease in reflected signal from 26-μm RS between 3 and 8 MHz illustrates narrowing spatial bandwidth. 52

Acknowledgments

The work reported herein has been performed under the sponsorship of the Aerospace Sciences Directorate, Air Force Office of Scientific Research; Dr Walter Jones and Capt Brian Sanders, PhD are the contract monitors. The experimental work during the program has benefitted from the generous loan and fabrication of characterized rough-surface samples made available by Prof Peter Nagy of the University of Cincinnati. As well, we would like to acknowledge helpful discussions on theoretical aspects of this work with Dr Jim Rose of the Iowa State Center for NDE. In the early stages of the project, Dr Ali Safaeinili made substantial contributions to this work, as well. In Sept 1995 he completed his postdoctoral fellowship and has since moved to a research staff position at the Rockwell International Science Center, Thousand Oaks, CA.

Executive Summary

In this Report is detailed the experimental and theoretical work performed to elucidate the propagation of guided elastic waves in plates with rough surfaces. The rough surfaces are taken as a model of incipient corrosion in aerospace structures. The work statement of this program is an agreed-upon abbreviated version of a three-year effort, as originally proposed. Below we list the proposed task items to be completed in this one-year effort, and directly thereafter we examine our accomplishments and compare them to the original goals of the program as proposed.

- Develop a model for guided plate wave propagation in plates with rough surfaces.
- Carry out experiments on plates with rough surfaces with shoe-type and knife-edge contact transducers.
- Characterize the plate roughness by independent acoustic profiling.
- Study the effect of the rough surface parameters on wave propagation and on the acquired experimental signal.

Reported here is the behavior of guided elastic waves in the presence of rough surfaces studied as a model of incipient corrosion. Extensive measurements in immersion, contact mode, and with knife-edge coupling demonstrate the wide range of physical behavior of elastic guided waves and their dependence on the condition of the guiding surfaces. These measurements have also led to a deeper understanding of challenges in finding optimal methods for the estimation of hidden surface roughness from ultrasonic guided wave measurements.

A simple, easily calculated, model of rough surface guided wave velocity dispersion has been developed, including all important roughness effects. The model is based on the phase-screen approximation, and plate waves are accommodated by applying the phase-screen approximation to partial wave reflections at each guiding surface. A rough surface dispersion relation is derived using transverse resonance, while extension to fluid-loaded plates is accomplished through a reflection series expression.

Comparisons between predictions of the model and experimental data demonstrate good agreement for all parameters investigated. Both in immersion testing, where predictable wave conversion at interfaces occurs, and also for contact mode coupling, accurate quantitative results have been deduced from the data, and these data agree remarkably well with the model predictions.

Essentially all the goals itemized above have been achieved, and in at least two areas, much more has been done than originally proposed. Highlighted accomplishments of the work reported herein are:

- A simple, yet highly accurate, model of guided wave propagation and attenuation in plates with rough surfaces has been derived;
- The model has been generalized to account for the more complicated case of propagation in plates with one rough surface only and loaded by a fluid, and this result has been incorporated into a rigorous voltage calculation; ⋆
- Many experiments have been performed to study rough surface guided wave effects in contact mode, and the difficulties of such measurements have been fully documented;
- Limited numbers of knife-edge measurements have been made, demonstrating the broad spatial spectrum expected of these transducers, but also opening new fruitful lines of investigation, since knife-edge experiments have shown very high sensitivity to roughness but reduced propensity for contact problems; ⋆
- Fully characterized samples have been used in every experiment;
- The full range of ultrasonic behavior in rough surface waveguides has been examined in immersion measurements, encompassing a wide range of values for many of the experimental parameters, including frequency, guided wave mode, incident angle, rms roughness, transmitter/receiver separation, roughness orientation;
- A clear demonstration of the importance of using guided elastic waves to characterize weak roughness over short lengths has been found by studying the plate rough-surface reflection coefficient, and this result is confirmed experimentally. ⋆

The ⋆ indicates additional unplanned progress.

1 Background

Recent DoD projections imply life extension of Air Force fleet aircraft well into the 21st century, making reliable early detection and characterization of hidden corrosion an important factor in safely extending the useful service life of today's aircraft fleet to meet the demands of a downsized Air Force.

One of the earliest effects of pitting or pillowing corrosion is the roughening of corroded surfaces. This roughening generally occurs long before any significant thinning takes place and is therefore an excellent indication of incipient reduction in structural integrity The most insidious aspect of corrosion is the damage it can do to the integrity of aircraft structure entirely out of sight of routine visual inspection. Lap and doubled butt joints in both wing and fuselage sections, with and without sealant, are subject to corrosion on hidden surfaces. In addition, the development of small subsurface cracks, particularly those emanating from fastener holes, can compromise structural integrity individually or, more insidiously, in concert with many other such subcritical defects through a phenomenon known as *wide-spread fatigue damage* [1]. In this latter case, the existence of many small fatigue cracks acts to reduce the residual strength of the overall structure, without any single defect exceeding a critical length. The net effect is to make the structure susceptible to failure from defects much smaller than the ASIP critical-length crack, predicted on the basis of a single crack in an otherwise sound structure.

The characterization of corroded materials in aircraft structure usually relies on the thinning or loss of material that accompanies the corrosion process. Ultrasonic characterization using guided waves can detect and quantify this material loss as well. However, a change in the surface roughness leads to increased wave damping which can be predicted analytically. But, there is another aspect to consider. Increased attenuation also affects the detectability of small defects in the structure, usually sited near fastener holes. Therefore, a further dimension is gained by examining the roughness of the hidden corroded surface using the attenuation or scattering of guided waves as a metric. When a guided wave propagates in a plate-like structure, its constituent partial waves scatter repeatedly from the surfaces of the guiding medium. This process, central to the propagation of guided waves, is also quite sensitive to the condition of the guiding surfaces, as we have recently demonstrated. Thus, guided wave ultrasonics can provide an "early warning system" for the incipient formation of hidden corrosion, at a point in time where the structure is still sound.

The problem of sound wave interaction with rough surfaces (RS) has attracted much attention in recent years, both theoretically and experimentally, owing to its significance in several fields. Scattering from wavy surfaces, seabeds and surface ice in ocean acoustics has been extensively dealt with, and here we can only hint at this literature. Moreover, rough surface scattering in dielectric waveguides, such as optical fibers, has also been widely researched. In either of these problems the fields can be assumed to be represented

by a single scalar potential. The problem we address here concerns the propagation of guided elastic waves in a planar solid waveguide having randomly rough surfaces with compressional and shear potentials that are coupled at each interface.

Most of the treatments of the acoustic rough-surface (RS) problem fall into two main categories: mean field integral transform methods [2]–[4], and perturbation methods [5]–[7]. There have also been studies of specific kinds of roughness, namely wave scattering at periodic surfaces [8]–[10]. Elements of wave scattering in a rough elastic layer have been treated in [11], but there is no consideration of guided waves. Each of the major approaches has its advantages and drawbacks. Those which are accurate under a broad range of conditions are also typically complicated to calculate with. Those that are easier to manipulate analytically may not give such accurate results for all wave components or in all parameter limits. There is, however, a simple approximate result for scattering from a randomly rough fluid-solid interface that can be conveniently expressed as a product of the zeroeth order (smooth surface) reflection coefficient and a simple function dependent on the wavelength and the roughness parameters. We will demonstrate that this approximate expression is, in fact, entirely sufficient as a basis from which to derive an initial estimate of scattering amplitude in guided elastic wave propagation.

Such an approximation was first introduced by Eckhart [12], in which the scattered field is taken to be composed of a random, incoherent component, owing to the RS scattering, and a residual coherent component. This approach, termed the phase-screen approximation (PSA), ignores any amplitude effects of the scattering and instead considers all the influence of the rough surface to be felt in the signal phase. Strictly speaking, the PSA is valid only in the Kirchhoff limit, when the elastic wavelengths in the solid are much larger than the rms roughness height h ($h << \lambda$), and when the fluid wavelength is much less than the roughness correlation length L ($\lambda_f << L$). This expression has also been derived by Ogilvy [13] and Nagy and Adler [14] from the Kirchhoff integral and has been discussed by Nagy and Rose [15], Ogilvy [16], and Dacol [17]. Using the PSA, comparisons to experimental measurements of fluid-solid RS ultrasonic scattering, in both transmission and reflection, have shown excellent agreement [14, 15].

The interaction can also be modeled using brute-force techniques such as the boundary integral equation method (BIE) [18]. However, the phase-screen approximation obtained from the Kirchhoff integral seems, in other applications, to work well enough to warrant the full investigation of its potential and limits of applicability before reaching for more complicated methods. In fact, as a nondestructive inspection tool, its simplicity makes it that much more attractive, so long as we can demonstrate its accuracy under conditions relevant to our problem of roughness characterization with guided waves.

The interaction of waves with rough surfaces has also been studied experimentally. These studies have focused on the attenuation and in some cases enhancement of the scattered wave. Nagy and Adler [14] have presented results on the attenuation of the transmitted and reflected wave for rough surfaces. They considered a reflection/transmission prob-

lem for a water/aluminum interface. They found that the transmitted wave is much less attenuated than the reflected wave. Furthermore, they noticed that the reflection from the back-surface of the plate is less attenuated than the front-wall reflection. This phenomenon is due to higher velocity in aluminum. This observation raises an important issue since this fact may suggest that for the plate application, one can reduce the effect of surface roughness conditions by exciting the wave on a smooth part of the surface. Once the wave is in the faster medium it is not affected as severely by the roughness, compared with a case where the wave is excited through a slower couplant on the RS.

Recently, Nagy and Rose [15] have examined the problem of detection of flaws located under a RS. They found that rough surfaces can cause serious degradation in the flaw signal-to-noise ratio, to the point where flaw detection is problematic. Bilgen [19] has studied the effects of focusing and flaw location in detection of flaws located under the RS. Other effects such as dependence of the transmission and reflection coefficients on the roughness parameters, for example correlation length, rms height, and incident angle are well known [13, 15, 19, 20].

There has been essentially no work, with the exception of our own recent studies, on the effect of rough surfaces on elastic guided waves. Significant efforts have been directed towards rough acoustic guides (fluid medium with solid boundaries) for ocean engineering [17, 16] and towards dielectric waveguides [21]–[25], where in each case only a single wave potential is sufficient to describe wave behavior in the propagating medium. In elastic solids the situation is much more complicated, since there are two wave potentials, and these are coupled to each other at every material interface.

2 Theoretical Development

We begin with a description of our theoretical approach and the derivation of a RS waveguide dispersion relation. In the second half of the section this approach is generalized to obtain a RS reflection coefficient for a plate having either one or two rough surfaces and immersed in liquid. We also demonstrate some properties of the solutions. Finally, we suggest in which directions the model must be extended to form the basis of an attack on practical inspection problems.

2.1 RS Waveguide Dispersion Relation

In elastic waveguide problems it is well known [26] that the guided wave mode can be decomposed into propagating or evanescent compressional and shear partial waves. To begin our discussion of the theory we present a calculation of the dispersion relation for an elastic waveguide with two rough traction-free surfaces. It proceeds from the assumption

we indicated above that we can use the phase-screen approximation to model the interaction of the partial waves with the rough surfaces. To derive a RS plate wave dispersion relation, we exploit the transverse resonance method [26] which naturally incorporates the partial wave reflection coefficients at the traction-free guide surfaces. The transverse resonance conditions for a smooth-surface plate are

$$\begin{aligned} A_p\, e^{-i\kappa_p d} &= A_p \Gamma_{pp}\, e^{i\kappa_p d} + A_s \Gamma_{ps} e^{i\kappa_s d} \\ A_s\, e^{-i\kappa_s d} &= A_p \Gamma_{sp}\, e^{i\kappa_p d} + A_s \Gamma_{ss}\, e^{i\kappa_s d}, \end{aligned} \tag{1}$$

where the partial wave compressional amplitude A_p and the shear amplitude A_s are functions of both compressional and shear halfspace reflection coefficients Γ_{pp} and Γ_{ss}, and the mixed coefficients Γ_{ps} and Γ_{sp}, since each partial wave both reflects and mode converts after interaction with the traction-free surface. The coefficients Γ_{ab}, where a and b can stand for p or s, are well known for the free halfspace. To modify this expression to accommodate rough surfaces, we need only introduce appropriate modifications in the scattering coefficients Γ_{ab}. Formally, this re-expression takes the form,

$$\begin{aligned} A_p\, e^{-i\kappa_p d} &= A_p \widehat{\Gamma}_{pp}\, e^{i\kappa_p d} + A_s \widehat{\Gamma}_{ps}\, e^{i\kappa_s d} \\ A_s e^{-i\kappa_s d} &= A_p \widehat{\Gamma}_{sp}\, e^{i\kappa_p d} + A_s \widehat{\Gamma}_{ss}\, e^{i\kappa_s d}, \end{aligned} \tag{2}$$

where $\widehat{\Gamma}_{ps}$ is the traction-free reflection coefficient for an incident compressional and reflected shear wave from a rough surface, and $2d$ is the plate thickness. Other similar terms $\widehat{\Gamma}_{ps}$, $\widehat{\Gamma}_{sp}$, and $\widehat{\Gamma}_{ss}$ are the scattering coefficients for indicated combinations of incident and reflected waves for a rough surface.

The transverse wavevector components (x_3 projection, in the plate normal direction) κ_p (compressional) and κ_s (shear) are given by $\sqrt{\omega^2/V_{p,s}^2 - \xi^2}$, respectively, where $V_{p,s}$ are the two indicated wavespeeds, ω is the angular frequency, and ξ is the wavenumber of the propagating guided wave (x_1 projection). The reflection coefficients (for coherent energy) $\widehat{\Gamma}_{\alpha\beta}$ ($\alpha = \{p, s\}$, $\beta = \{p, s\}$) for a RS are given, according to the phase-screen approximation (PSA), by a product of the zeroeth (smooth surface) coefficient $\Gamma_{\alpha\beta}$ and the PSA contribution,

$$\widehat{\Gamma}_{pp,ss} = \Gamma_{pp,ss}\, e^{-2h^2\kappa_{p,s}^2} \tag{3}$$

$$\widehat{\Gamma}_{ps,sp} = \Gamma_{ps,sp}\, e^{-h^2(\kappa_p+\kappa_s)^2/2}. \tag{4}$$

For convenience let ε, λ, and δ be defined as follows,

$$\begin{aligned} \varepsilon &= \exp[-2h^2\kappa_p^2] \\ \delta &= \exp[-2h^2\kappa_s^2] \\ \lambda &= \exp[-h^2(\kappa_p + \kappa_s)^2/2], \end{aligned} \tag{5}$$

The expressions in Eqs. (3)–(5) can be substituted into Eq. (2), yielding a homogeneous linear system for the wave amplitudes $A_{p,s}$ that will have a nontrivial solution if

$$\det \begin{vmatrix} \varepsilon\Gamma_{pp}\, e^{i\kappa_p d} - e^{-i\kappa_p d} & \lambda\Gamma_{ps}\, e^{i\kappa_s d} \\ \lambda\Gamma_{sp}\, e^{i\kappa_p d} & \delta\Gamma_{ss}\, e^{i\kappa_s d} - e^{-i\kappa_s d} \end{vmatrix} = 0. \tag{6}$$

The Γ_{ab} scattering coefficients can be reduced to a single term Γ_{pp} using the following relations

$$\begin{aligned} \Gamma_{ss} &= -\Gamma_{pp} \\ \Gamma_{sp}\Gamma_{ps} &= (1-\Gamma_{pp}^2) \end{aligned} \tag{7}$$

among the coefficients. Carrying out the determinant and collecting terms, we have that

$$\begin{aligned} \varepsilon\delta\Gamma_{pp}^2\, e^{i(\kappa_p+\kappa_s)d} + \varepsilon\Gamma_{pp}\, e^{i(\kappa_p-\kappa_s)d} - \delta\Gamma_{pp}\, e^{-i(\kappa_p-\kappa_s)d} \\ + \lambda^2(1-\Gamma_{pp}^2)\, e^{i(\kappa_p+\kappa_s)d} - e^{-i(\kappa_p+\kappa_s)d} = 0\,. \end{aligned} \tag{8}$$

This is the dispersion relation for a RS waveguide using the PSA scattering model to treat the effective attenuation of guided mode partial waves as they interact with the surface. This relation has been derived here for elastic waveguides for the first time, to our knowledge. Limitations of the phase-screen model, on which this calculation is based, are its independence of the correlation length L and its assumption of a Gaussian roughness distribution. A further aspect of the PSA model is that it consciously models only the coherently reflected signal, neglecting the incoherent component. For our purposes this selection makes perfect sense, and may explain why so little work on the rough elastic waveguides exists in the literature. For ultrasonic NDE measurements the usual transmitter and receiver is a baffled piston radiator some several wavelengths or more in diameter. The directivity afforded by the transducer radius and its uniform piezoelectric vibrational mode may be added to the wavenumber/frequency selectivity of the guided waves in sample plate itself. Together, these effects strongly militate against a latent sensitivity to the incoherent component of the scattered field. Therefore, we may confidently ignore the incoherent field in favor of the one modeled in the PSA, the coherent field. This is a great advantage for our measurements and modeling simplicity. In ocean acoustic engineering, by contrast, the sound sources and receivers are typically a small fraction of a wavelength, essentially point sources. In this circumstance the contributions from the incoherent field are not necessarily negligible, and must be considered in a realistic model.

Solutions of Eq. (8) are best studied graphically. In particular, it is instructive to examine the trajectory of the pole of Eq. (8), *ie* the complex guided wavenumber ξ as a function of frequency. With a smooth surface the imaginary part of ξ will vanish in the absence of material losses. In the case we consider here, the nonzero imaginary wavenumber $\mathrm{Im}(\xi)$ arises because of the effective attenuation incurred as the partial waves reflect from the rough guide surfaces. Figure 1 shows pole trajectories in the complex plane for three antisymmetric modes, beginning with A_4 plotted as a parametric function of frequency.

Several features deserve mention. The large increase in imaginary wavenumber near each mode cutoff has a clearly intuitive explanation. As the mode approaches cutoff, the partial wavevectors are oriented nearly normal to the plate surface, implying many reflections per wavelength and leading to a large increase in surface-induced losses. At slightly higher

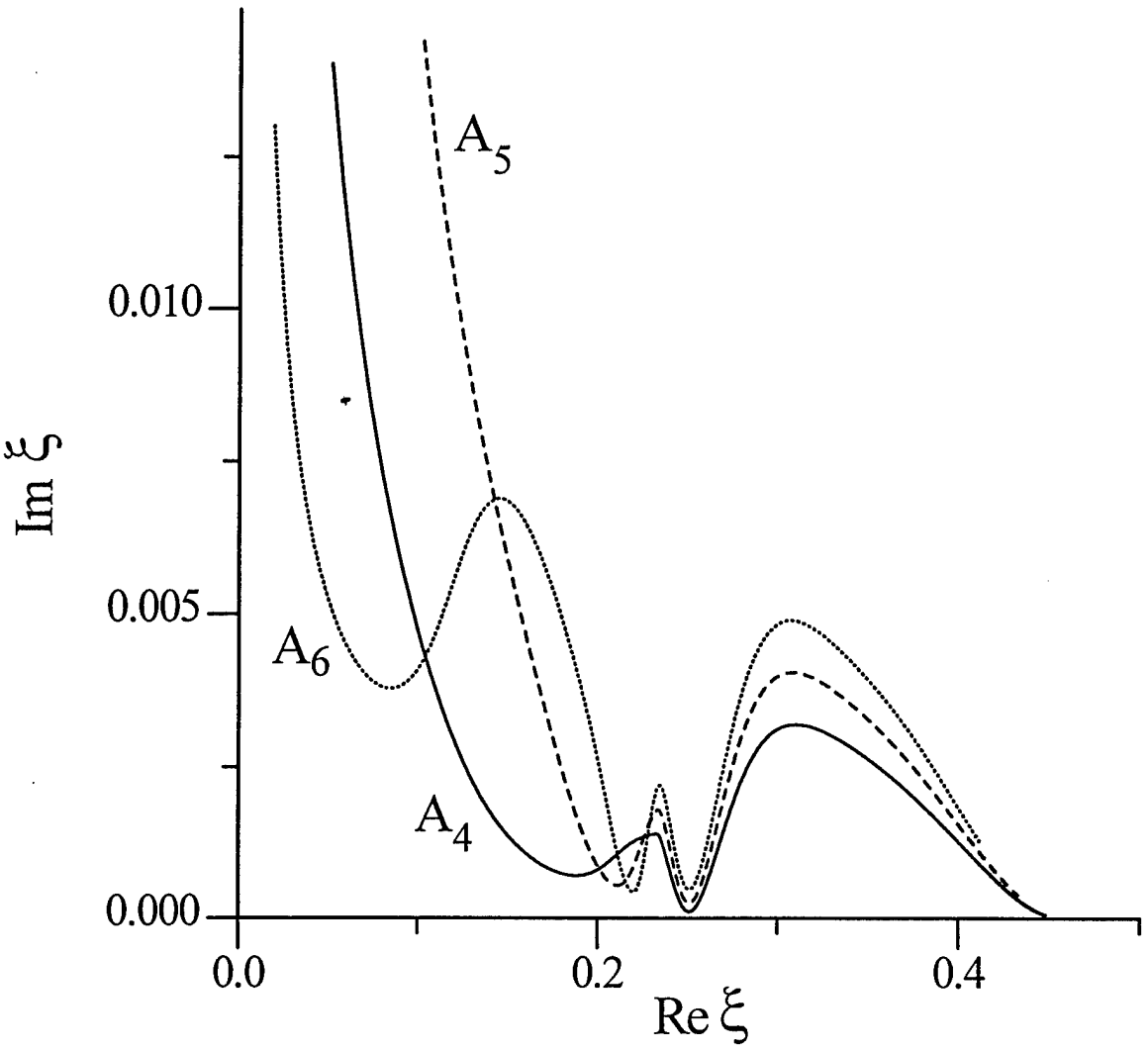

Figure 1: Pole trajectories in the complex plane for several antisymmetric plate modes, showing strong dependence of damping part on incident angle. Inset shows experimental geometry and defines axes.

frequency, for each mode, $\mathrm{Im}(\xi)$ falls, increases, and falls to a low value, after which it increases and again decreases towards $\mathrm{Im}(\xi) = 0$. We may explain this behavior by noting it occurs close to the compressional critical angle. Near this branch point of the function in Eq. (8) conversion of compressional to shear wave energy achieves a local maximum, compared to its value on either side of the critical wavevector. Farther along the pole trajectory, the p wave ceases to be a factor, and the s-wave damping increases. At higher frequency still, the s partial wavevector approaches its critical value and makes progressively larger angles with the plate normal, and the partial wave interaction with the rough surface decreases as the modes approach their real limiting value, the shear wavenumber κ_s.

This last aspect of the model, the vanishing of roughness-induced damping at large angles, is not entirely realistic, but does approximate experimental observations. What is happening in our model is that the partial waves contribute to the surface-induced losses only to the extent that their ray path brings them into contact with the rough surface. If this event does not (or only rarely) occur, as in the case of the evanescent compressional wave or the shear wave near Lamb wave limiting velocity, then the model predicts a consequent reduction of RS damping. To pursue this question further would take us into the interesting, but more challenging, realm of the analysis of surface waves on a rough surface. Here, the problem we are now skirting is met head on. For Rayleigh surface waves both partial wave components are evanescent; it is the essence of a surface-bound excitation. By analogy to the cases of other loss mechanisms, it might be expected that Rayleigh waves would become "leaky" into the bulk at some critical damping value. This condition could be achieved through variations in either the rms roughness or frequency. While fascinating to speculate on, these matters are not centrally pertinent to the work at hand. In the current case, fortunately, operation near the limiting value κ_s is seldom useful for materials inspection with plate waves.

There are some interesting limits of Eq. (8) worth investigating. The first concerns the comparative values of exponents in Eq. (6a) and Eq. (6b). If the Poisson ratio is greater than about 0.3, the compressional wavespeed will be at least about twice the shear value. This ratio implies that the effect of δ in Eq. (6b) will dominate over ε. Therefore, to good approximation we can write $\varepsilon \approx 1$ and $\lambda^2 \approx \varepsilon\delta \approx \delta$. With this substitution we have

$$\Gamma_{pp}\, e^{i(\kappa_p-\kappa_s)d} - \delta\Gamma_{pp}\, e^{-i(\kappa_p-\kappa_s)d} + \delta\, e^{i(\kappa_p+\kappa_s)d} - e^{-i(\kappa_p+\kappa_s)d} = 0\,. \tag{9}$$

This equation can be further reduced by incorporating the δ terms as real parts of the exponential arguments, which leads naturally to a redefinition of one of the parameters d as an effective complex halfthickness $\tilde{d}$, whose imaginary part introduces the lossy rough surface contribution. In this way the rough surface dispersion relation can be expressed formally in the same manner as the ordinary Lamb wave equation, but with a complex thickness parameter. As expected, if the rms roughness parameter h goes to zero, we recover the ordinary Lamb wave equation.

2.2 Generalized Scattering Coefficients for RS Plate

To apply our model, based on the PSA, to immersion reflection measurements it is essential to have a generalized model of plane wave interaction with RS plates. Considering our experimental samples and the kinds of measurements we have made, the expression in Eq. (8) will only be useful if recast into the form of scattering (reflection and transmission) coefficients. With samples having roughness on one side only, a different dispersion relation is needed, and the collateral reflection coefficient must differentiate between RS facing towards the transducers and away from them. The difference in the immersion measurements is substantial. The reflected wave amplitude consists of two rather distinct contributions. One comes from the wave reflected at the upper plate surface, essentially a specular reflection, and the other is the leaky guided wave that suffers reradiation as it propagates. Both components will be affected by the roughness, but each in a different way.

The specular signal reflected back into the fluid medium where the wavelength is small (owing to the low fluid compressional wavespeed), is substantially reduced by interaction with the rough surface, whereas the guided wave interacts in the way described earlier. One additional complication is that for the RS facing upwards, the guided wave must reradiate *through* this surface, additionally complicating the signal. With the RS on the bottom (facing away from the transducers), only the guided wave signal can feel the influence of the roughness, according to the dispersion relation derived above.

To construct a plate reflection coefficient (RC) from the halfspace rough surface reflection coefficients, we begin with a derived expression for the plate RC using joined halfspace scattering coefficients,

$$R = R_h + \frac{T_p\left(\tau_{pf}\left(1-\tau_{ss}\right)+\tau_{sf}\tau_{ps}\right)+T_s\left(\tau_{sf}\left(1-\tau_{pp}\right)+\tau_{pf}\tau_{sp}\right)}{\left(1-\tau_{pp}\right)\left(1-\tau_{ss}\right)-\tau_{ps}\tau_{sp}} \tag{10}$$

where R_h and T_p and T_s are the joined halfspace reflection and compressional and shear transmission coefficients for a fluid-solid interface. We have used R and T here instead of Γ from the earlier section to distinguish between a halfspace RC, where the material interfaces to a vacuum, and the joined halfspace RC, where two acoustic media meet at a planar interface, in this case fluid and solid. It is also understood that, as above, R_h and $T_{p,s}$ are the rough-surface equivalents in the phase-screen approximation to their counterparts in the absence of roughness. The term in Eq. (10) $\tau_{\alpha\beta}$ refers to the following RC products,

$$\tau_{\alpha\beta} = R^{II}_{\alpha p}R^{I}_{p\beta} + R^{I}_{\alpha s}R^{I}_{s\beta} \tag{11}$$

with $\alpha = \{p, s\}$ and $\beta = \{f, p, s\}$ (f: fluid), as before, and $R^{I,II}_{\alpha\beta}$ are reflection and transmission coefficients on solid-fluid interfaces I and II. The explicit rough-surface dependence is

$$\widehat{R}_h \;=\; R_h e^{-2h^2\kappa_f^2}$$

$$\begin{aligned} \widehat{R}^{I,II}_{\alpha\beta} &= R^{I,II}_{\alpha\beta} e^{-h^2(\kappa_\alpha+\kappa_\beta)^2/2} \\ \widehat{T}_p &= T_p e^{-h^2(\kappa_p+\kappa_f)^2/2} \\ \widehat{T}_s &= T_s e^{-h^2(\kappa_s+\kappa_f)^2/2} . \end{aligned} \tag{12}$$

(13)

To accommodate rough upper or rough lower fluid-loaded plate surfaces, the appropriate RS reflection $\widehat{R}$ and transmission $\widehat{T}$ coefficients are inserted in Eq. (10) in place of their smooth surface counterparts.

The six coefficients $\tau_{\alpha\beta}$ represent two successive reflections and transmissions of an incident plane wave of type α on interface II, as shown in Fig. 2. Thus, after a further reflection, this wave again yields a plane wave of type β at interface I. In other words, these coefficients provide two possibilities for obtaining a wave type α from wave type β. For illustration, Fig. 2 shows the cases for the coefficients τ_{ss} and τ_{pf}.

The reflection and transmission coefficients $R^{(1,2)}_{\alpha\beta}$ (α is an incident wave and β is a reflected or transmitted wave) on the solid-fluid interfaces I and II are [26]

$$\begin{aligned} R^{I,II}_{pf}(\xi) &= \frac{2\kappa_p k_s^2 (k_s^2 - 2\xi^2)}{\kappa_f D} e^{i\varphi_p}, \\ R^{I,II}_{ps}(\xi) &= -\frac{4\xi\kappa_p (k_s^2 - 2\xi^2)}{D} e^{i(\varphi_p+\varphi_s)}, \\ R^{I,II}_{pp}(\xi) &= \frac{-(k_s^2 - 2\xi^2)^2 + 4\xi^2\kappa_p\kappa_s + Y}{D} e^{2i\varphi_p}, \\ R^{I,II}_{sf}(\xi) &= \frac{4\xi\kappa_p\kappa_s k_s^2}{\kappa_3 f D} e^{i\varphi_s}, \\ R^{I,II}_{sp}(\xi) &= -\frac{4\xi\kappa_s(k_s^2 - 2\xi^2)}{D} e^{i(\varphi_p+\varphi_s)}, \\ R^{I,II}_{pp}(\xi) &= \frac{(k_s^2 - 2\xi^2)^2 - 4\xi^2\kappa_p\kappa_s + Y}{D} e^{2i\varphi_s}, \\ R_h(\xi) &= \frac{(k_s^2 - 2\xi^2)^2 + 4\xi^2\kappa_p\kappa_s - Y}{D}, \\ T_p(\xi) &= \frac{2\rho k_s^2 (k_s^2 - 2\xi^2)}{D} e^{i\varphi_p}, \\ T_s(\xi) &= \frac{4\xi k_s^2 \kappa_p}{D} e^{i\varphi_s}. \end{aligned} \tag{14}$$

(15)

Here,

$$D = (k_s^2 - 2\xi^2)^2 + 4\xi^2\kappa_p\kappa_s + Y \tag{16}$$

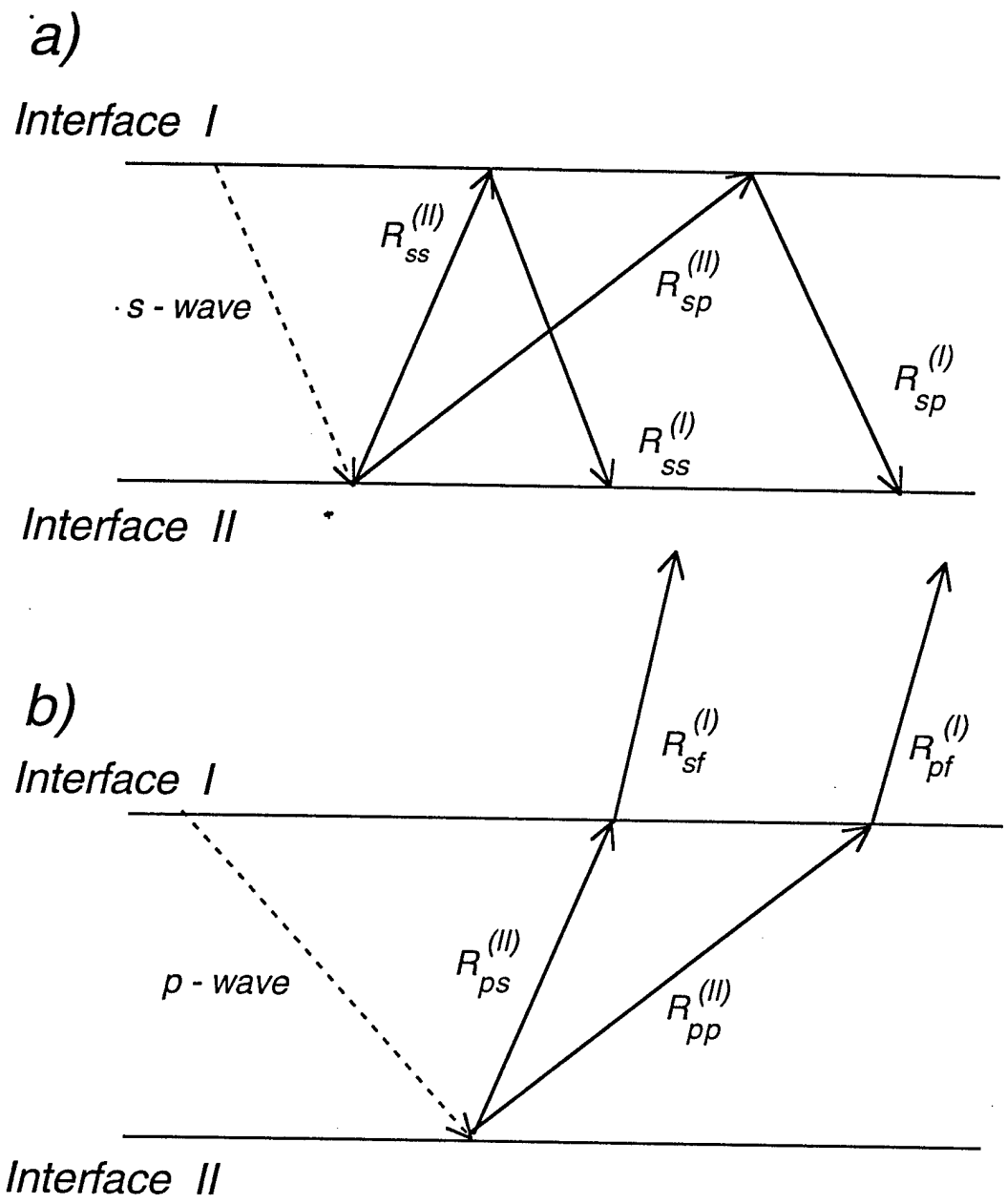

Figure 2: Reflection series for an internally incident s and p wave in a plate. In b) wave leakage is illustrated at the upper plate surface.

is denominator of the RC expressions, $\varphi_{p,s}$ are the compressional and shear wave propagators, and Y is the fluid term given by

$$Y = \frac{\rho_f}{\rho} \frac{k_s^4 \kappa_p}{\kappa_f}, \tag{17}$$

where compressional and shear wavenumbers are $k_p (= \omega/V_p)$ and $k_s (= \omega/V_s)$, and ξ is the x_1 wavevector projection onto the plate surface. In isotropic materials, these definitions imply $k_{p,s}^2 = \xi^2 + \kappa_{p,s}^2$. The wavevector projection onto the plate surface is ξ an invariant quantity. The fluid and solid material densities are ρ_f and ρ.

The most direct way to see the effect of rough guiding surfaces on the behavior of plate waves is to examine the reflection coefficient. This quantity contains all the material property information, including surface condition, pertaining to the plate. The measured signal can, of course, differ sharply from the RC, owing to the effects of diffraction and experimental geometry. This critical point is the essence of the analysis presented in [27] and discussed further below. For now, let us look at two reflection coefficients, one for roughness on the upper plate surface, Fig. 3, and the other for roughness on the lower surface, Fig. 4.

In Fig. 3 the effect of the roughness is very pronounced since both specular and reradiated components of the signal interact with it. For $h = 30$ μm the RC magnitude has characteristic minima at low frequencies where propagating guided modes exist. These interfere with the specular component and lead to RC minima. At higher frequencies the minima are less deep, and finally above 8 MHz they become small but growing peaks. Why is this? The roughness on the top surface becomes a much stronger influence ($\exp(-2\kappa_f^2 h^2)$) at high frequency, severely attenuating the specular wave, so that additive influence of the resonant guided wave is now seen as an increase in reflected energy. At $h = 100$ μm this behavior is very well developed, and only a single minima near 2 MHz can be discerned. Beyond 7 MHz the damping of plate resonances is so strong, that virtually no energy is reflected.

Very different behavior is seen for roughness on the bottom surface in Fig. 4; the $h = 0$ μm curve is repeated for comparison. At $h = 30$ μm both the depth of the minima and the intervening maxima are reduced as the frequency grows. With roughness on the lower surface, only the reradiated guided wave can feel its influence. So, the roughness acts in this case only as a "Q spoiler", effectively broadening the plate acoustic resonances. The natural effect of this resonance broadening will be the imperfect phase cancellation and reinforcement of the unaffected specular signal at both the minima and maxima, respectively. This effect explains why the resonance minima are progressively less deep, and why the maxima no longer reach all the way to unity. Eventually, for $h = 100$ μm, the roughness spoils the quality factor or "Q" of the acoustic resonances so badly that above 8 MHz only the constant specular component remains. The rest of the acoustic energy is dissipated (dephased in the PSA) in one or two interactions with the lower (rough) plate surface.

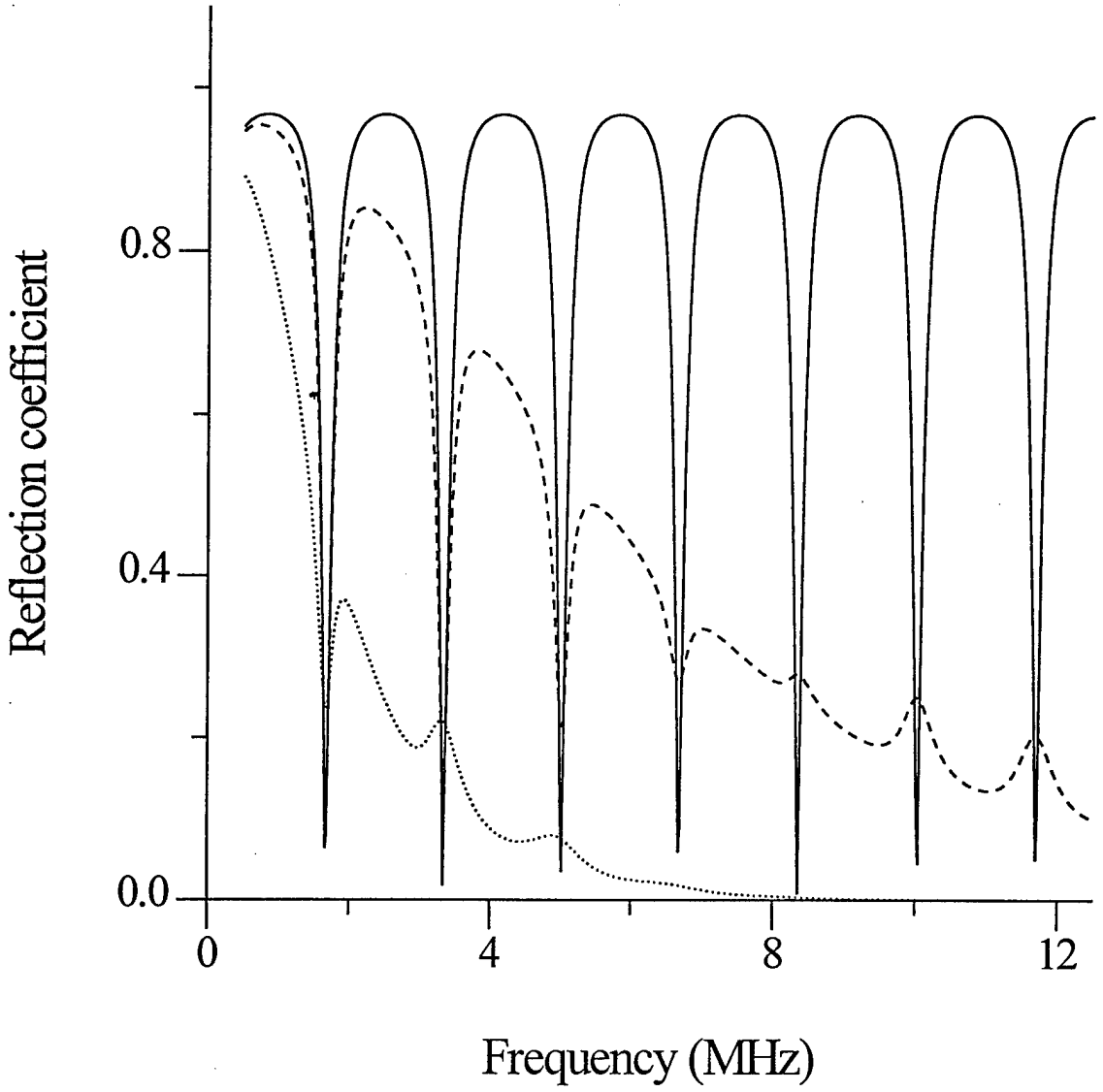

Figure 3: Plane wave reflection coefficient magnitude for progressively increasing roughness on the upper plate surface (facing transducers); rms roughness $h = 0$ (solid curve), $h = 30$ μm (dashed), and $h = 100$ μm (dotted). Plate thickness is 1.37 mm and incident angle is 20°.

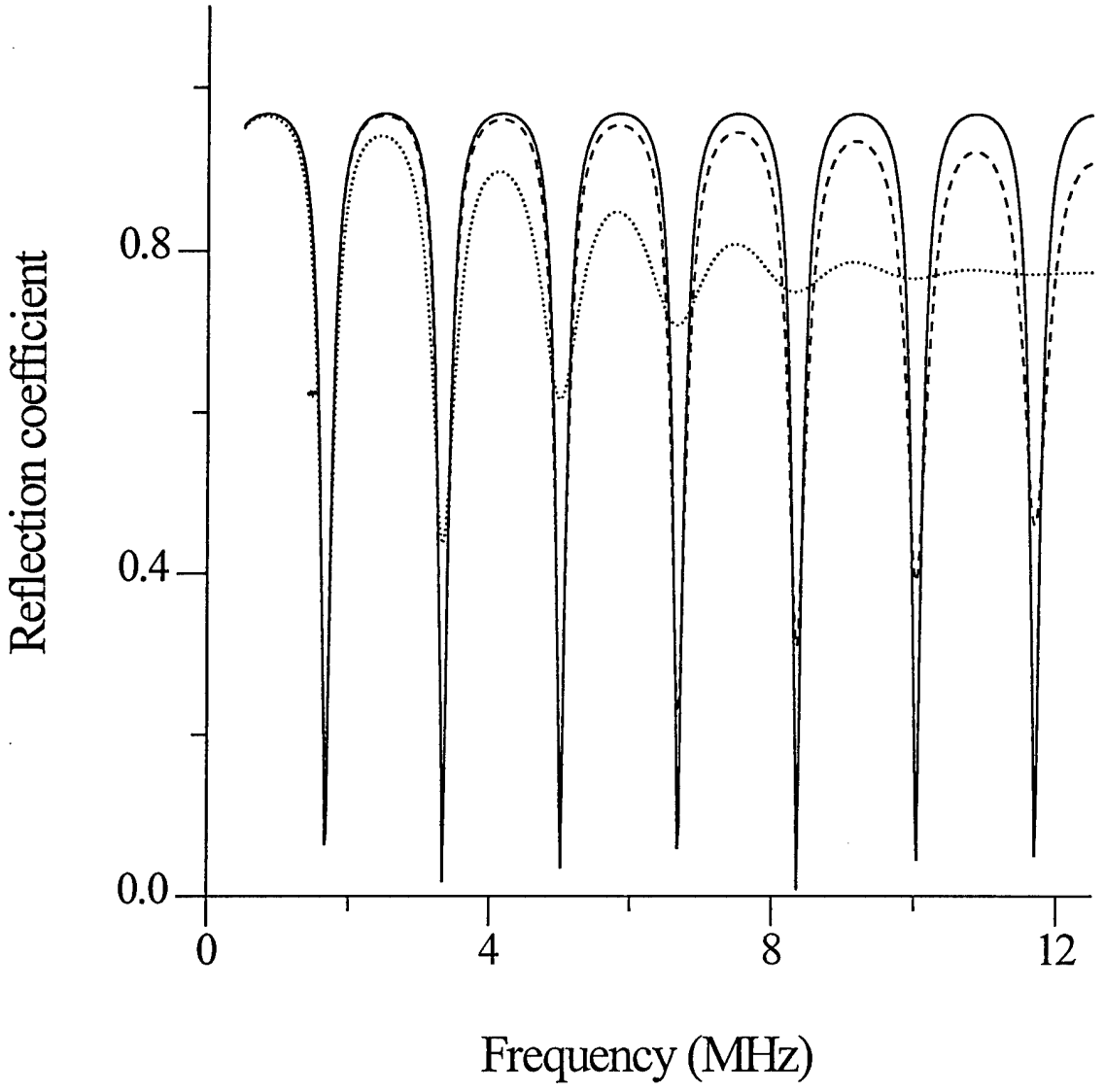

Figure 4: Plane wave reflection coefficient magnitude for progressively increasing roughness on the lower plate surface (away from transducers); rms roughness $h = 0$ (solid curve), $h = 30$ μm (dashed), and $h = 100$ μm (dotted). Plate thickness is 1.37 mm and incident angle is 20°.

This last plot, especially, illustrates the importance of examining guided wave behavior to elucidate roughness on hidden surfaces. When the roughness is exposed, as in Fig. 3, its effect on the ultrasonic signal is strong and obvious, as found by Rose and Nagy [15]. But, practically speaking, roughness in this case can be detected by visual examination—no high-tech methods are needed. When, however, the roughness is hidden, as in Fig. 4, straightforward ultrasonic reflection measurements, exemplified by the RC behavior, are hardly sufficient to detect any but the grossest roughness (h=100 μm). Even then, the difference between smooth and rough is only about 20% in the absolute RC magnitude, hardly an unequivocal indicator of roughness. By contrast, the guided waves demonstrate a *much* larger effect from the roughness, as we will see below. This happens because the guided mode partial waves interact many times with the surface as they propagate, giving them a greater sensitivity to roughness (corrosion) in plate-like structures than virtually any other ultrasonic wave type.

A different way of looking at these calculated reflection coefficients is seen in Figs. 5 and 6. In Fig. 5 the reflection coefficient for a rough *lower* surface, opposite the incident wave, is shown as a function of angle at 8 MHz instead of frequency for three different rms roughnesses, $h = 0,\ 30,\ 100\,\mu$m. Recalling the behavior in the pole trajectories shown in Fig. 1, the greatest losses occur near 15°, where the curves have the shallowest minima and the lowest maxima. As the angle increases towards the shear critical angle of 30°, the RS damping contribution vanishes. Past 30°, there is no RS effect. This plot illustrates most clearly, perhaps, the one unrealistic aspect of the PSA-based guided wave RS model: damping ceases when the wave becomes evanescent. For guided plate waves, this may not be too serious, since the shear partial takes over and contributes to the losses past the compressional critical angle. And as we pointed out earlier, Lamb waves are seldom used near the shear limiting wavespeed, because all modes pile up at this accumulation velocity, and distinguishing among them can be difficult. The problem comes in consideration of the A_0 mode, whose entire dispersion branch lies in the region where both partial waves are evanescent. This statement pertains also to Rayleigh surface waves, whose partial waves are all evanescent.

The corresponding plot for the rough surface on the same side as the incident plane wave is shown in Fig. 6 for rms roughnesses $h = 0,\ 15,\ 30\,\mu$m. The upper rough surface dephases the specular wave, and the roughness effect is much more pronounced for much smaller roughness. These data further amplify the importance and utility of guided wave measurements to elucidate roughness parameters in plate-like structure. The frequency is again 8 MHz. The reduction in the specular reflection is strong enough at $h = 30\,\mu$m that the guided wave resonances again appear as peaks in the calculated RC. With top surface roughness the RS contribution does not vanish past the internal shear critical angle. However, as the incident angle α increases, the magnitude of the RC does approach unity. This is also observed and predicted for the much more complicated case of grazing incidence in rough surface acoustic scattering.

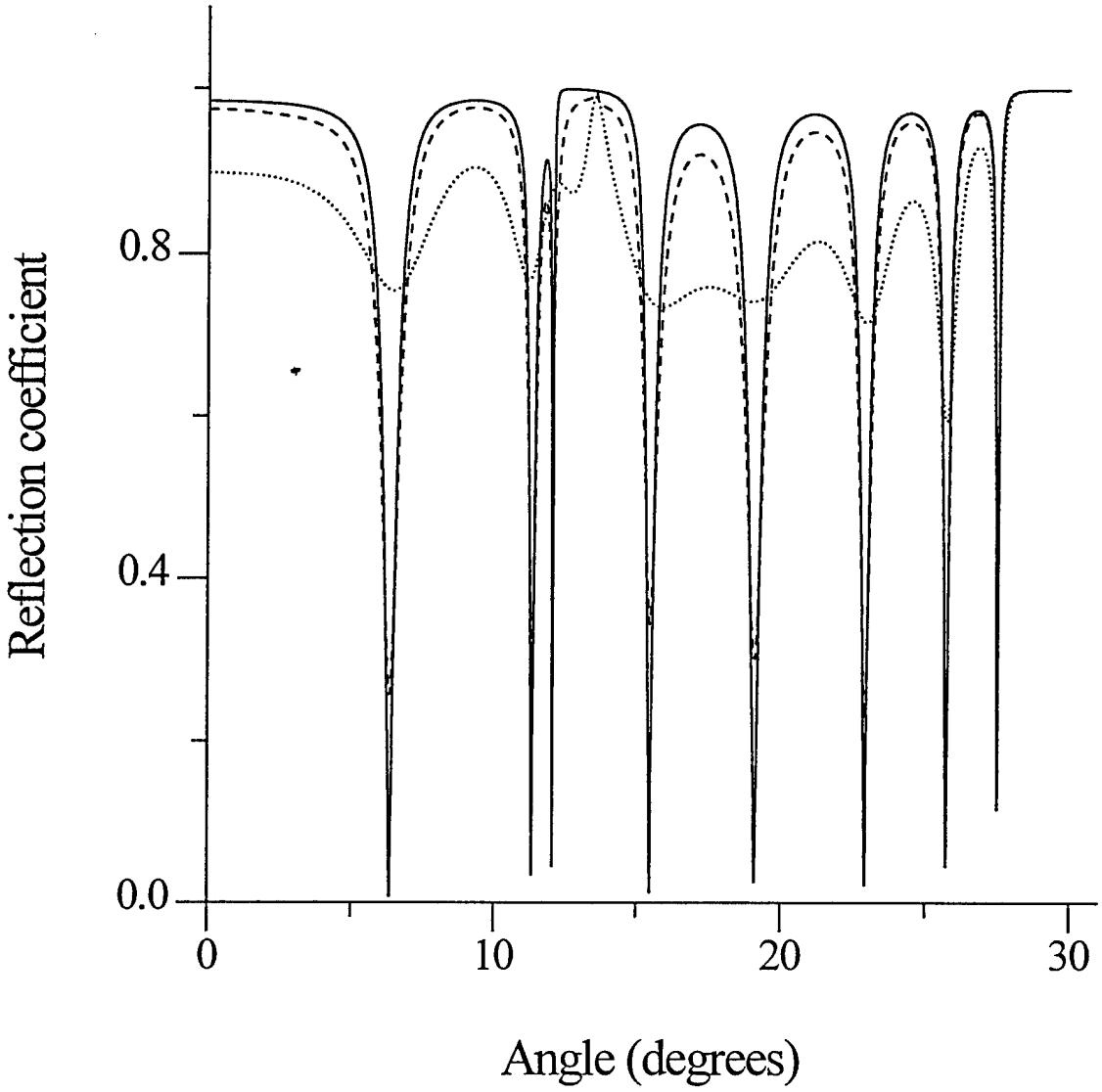

Figure 5: Plane wave reflection coefficient magnitude for progressively increasing roughness on the lower plate surface (away from incident wave); rms roughness $h = 0$ (solid curve), $h = 30$ μm (dashed), and $h = 100$ μm (dotted). Plate thickness is 1.37 mm and fixed frequency is 8 MHz.

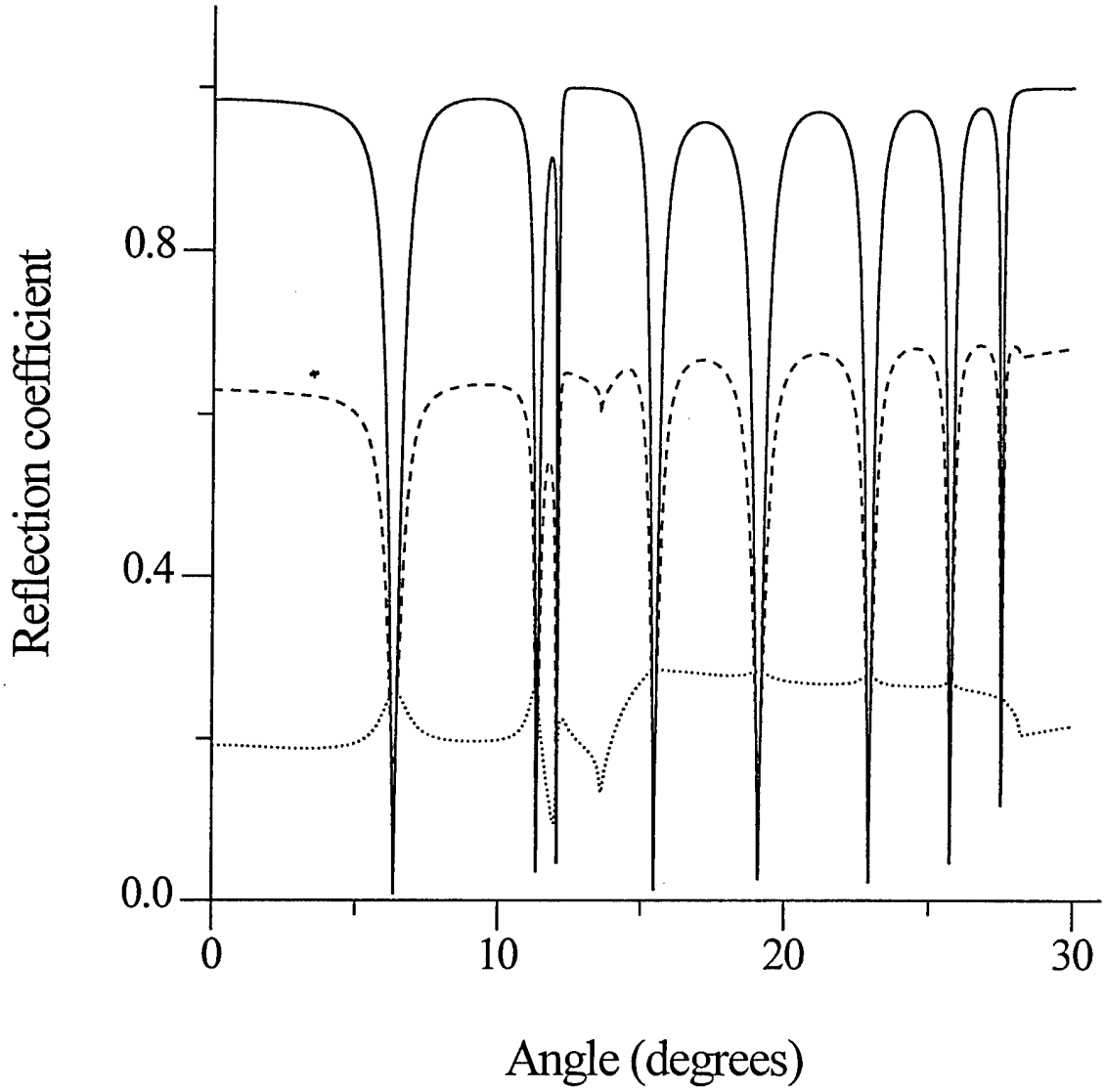

Figure 6: Plane wave reflection coefficient magnitude for progressively increasing roughness on the upper plate surface (towards incident wave); rms roughness $h = 0$ (solid curve), $h = 15$ μm (dashed), and $h = 30$ μm (dotted). Plate thickness is 1.37 mm and fixed frequency is 8 MHz.

3 Experimental Technique

Many experiments have been performed in this work to elucidate the rough surface damping phenomena in plates and to examine the potential of the analysis to make accurate predictions of guided wave propagation its eventual usage in deducing roughness from inspection measurements. We show here only processed spectra and coordinate scans, since data are collected as either video-detected tone bursts or time-domain sampled tone bursts. Signals in all cases have ample signal-to-noise ratios for all but the highest frequency and the largest transducer offset.

Broadband piezoelectric piston transducers are excited with tone burst rf signals 50-μs in length, with or without power amplification. The acoustic wave generated in this way interacts with the plate and is reradiated into the fluid, where it is detected by a second, nominally identical device. This detected signal is amplified and either envelope-detected by an rf receiver or passed to a digital oscilloscope for capture and analysis. In the computer the time-domain signal is generally Fourier transformed in order to isolate a particular frequency component from the narrow, but finite bandwidth burst. This operation is nominally equivalent to video envelope detection of the burst followed by boxcar integration and dc sampling. The transform method, although more time-consuming, results in a cleaner waveform, less influenced by out-of-band signal energy. A block diagram of the experimental apparatus is shown in Fig. 7.

Two fundamentally different kinds of measurements have been made in this work. One kind is done in contact mode, either with wedges or with knife-edges; the other is done in immersion. In the immersion testing, transducers are aligned by observing the amplitude of signals reflected from sample surfaces and by precise mechanical measurements of transducer spatial relationships. Incident angles are selected by optical rotation stages, lending high accuracy and resolution to the experiments. We then perform measurements with the scanning bridge and all experimental instruments operating under computer control. In contact mode, transducers are also aligned with signal amplitude, and a miniature precision scan apparatus is used to make transducer position adjustments on the 10 μm scale level. While every effort is made to suppress the disturbing effect of variable contact efficiency, the plate fabrication methods left some surfaces not quite flat, further complicating the measurements. For these reasons, many averages are made to lessen the influence of variable contact. Contact force, couplant thickness, and other geometrical parameters are controlled as far as possible. However, some variability remains. Data acquisition is rapid and precise, even allowing for some averaging of the digitized signal, in order to minimize the effects of gain variation, temperature fluctuations, or instrument drift. The samples are oriented with their rough surfaces either towards or away from the transducers in the immersion measurements. Generally, averages of several measurements made at different positions are used to obtain as representative a sampling of the surface roughness as possible. A schematic diagram of the immersion experimental setup is shown in Fig. 8, and the contact measurements are illustrated in Fig. 9.

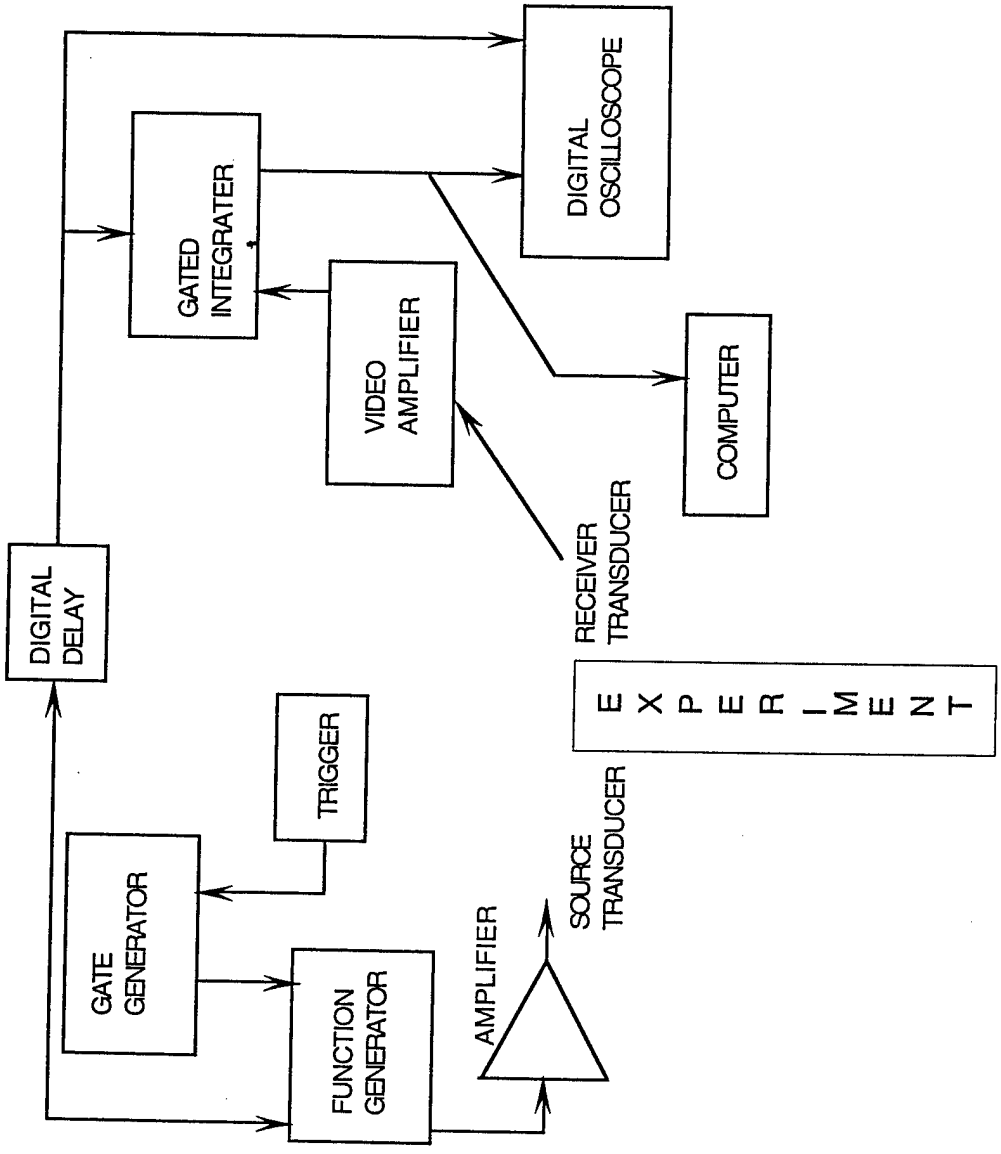

Figure 7: Block diagram of experimental apparatus, showing signal generation and detection channels.

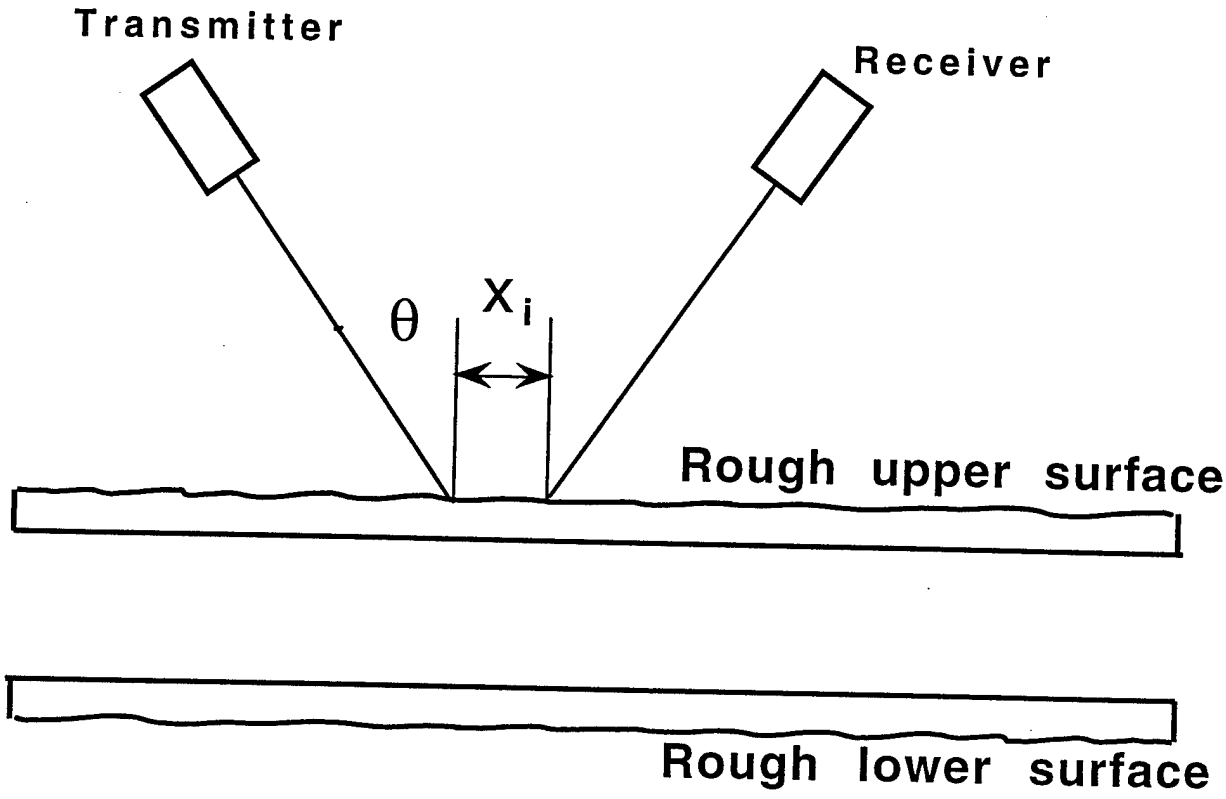

Figure 8: Schematic diagram of immersion experiments showing the deployment of the transducers and the parameters varied.

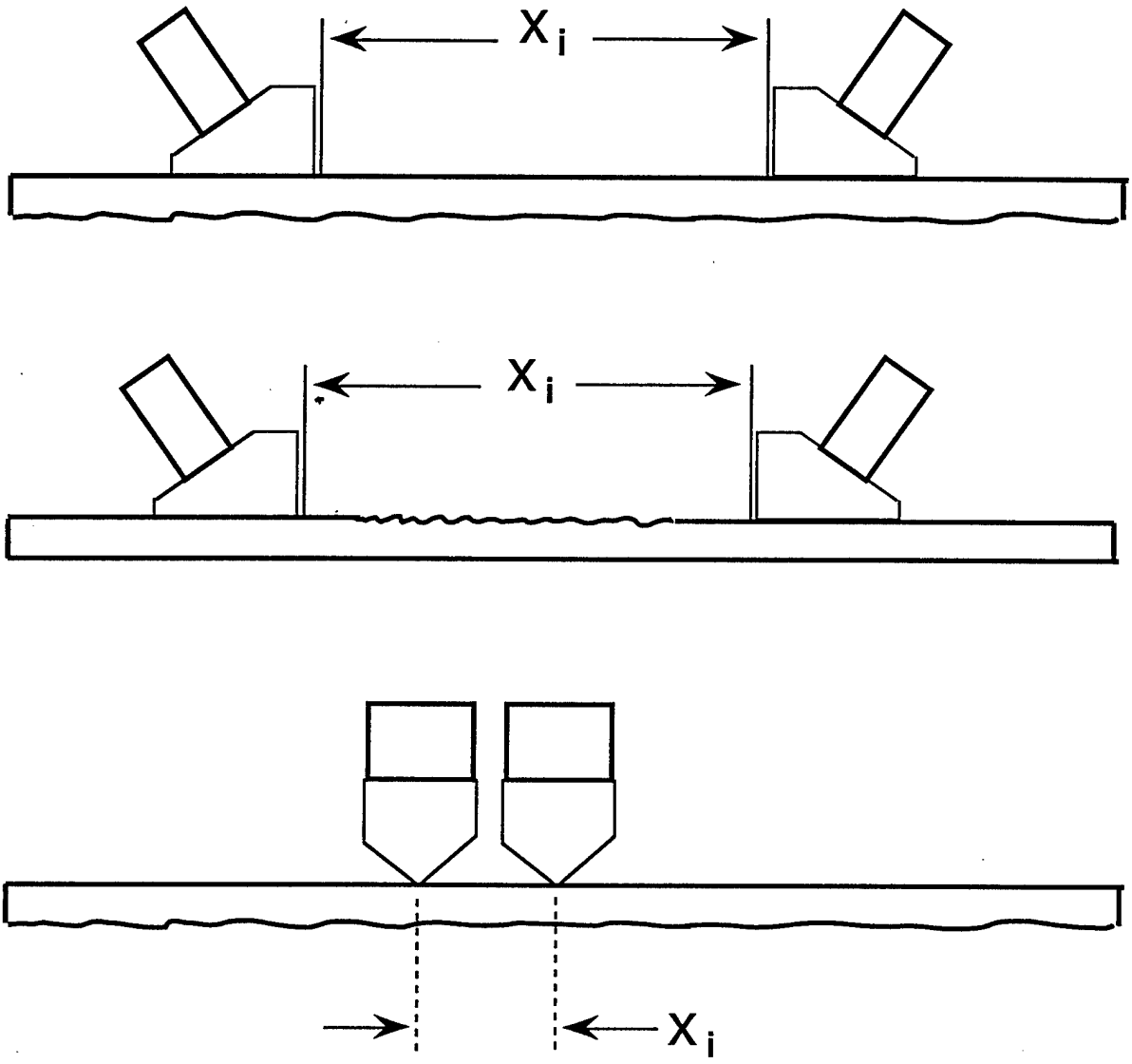

Figure 9: Schematic diagram of contact experiments showing the deployment of the transducers and the parameters varied.

Samples for this study have been fabricated in one of two ways. Since we model surface roughness as a random distribution of surface height with a well defined mean and variance, we seek in our samples a nearly Gaussian distribution of roughness. This goal can be accomplished either with a chaotic bombardment of small particles, such as sandblasting, or with a pseudorandom indenting machine, where careful deterministic calculations are performed to construct an approximately random surface roughness. All samples are fabricated from aluminum, but the indented specimens (which have a higher rms roughness) must be made from 1100 series alloy to permit the indenter to have any substantial effect. The sandblasted samples are selected from a series of 9-mm thick Al-2024 plates used in a previous study [15]. They have been well characterized by acoustic microscopy. Their method of fabrication is not, however, as well controlled as the indented specimens. From the set of samples a smooth plate, a midsize roughness, and a high roughness plate have been selected.

To render these effective halfspaces useful for our purposes, each sandblasted sample has been milled from the back surface, opposite the roughness, until a desired smaller thickness is attained. Then, to relieve any residual stresses that might warp the plates, each plate (2.3 or 1.4 mm) is annealed at 500°F under static pressure and slow cooled to room temperature. After this treatment, the flatness of the plates is tested on a reference surface. In most cases no residual warping can be detected. A similar treatment is also applied to the indented samples, which respond very well since they are unalloyed aluminum. For our experimental purposes the aluminum alloy composition is of little significance. The measurements yield identical results in either the 1100 series alloy or the precipitation hardened Al-2024.

4 Results and Discussion

In this section we present sets of plots on the three types of measurements performed in this project: immersion, contact, and knife-edge. Since a major goal in this one-year program was to clarify our understanding of guided wave damping effects in the presence of surface roughness, other sources of error should be reduced to the minimum. Therefore, most of the critical comparisons between experiment and prediction and most of the exploration of rough surface phenomenology has centered on experimental investigations using reliable immersion coupling methods. In most cases we show results in tandem, experiment and theory, to illustrate the effect of rough surfaces on guided waves in plates and how this effect can change with different measurement conditions. Accompanying each plot of experimental data is a corresponding prediction of the approximate model discussed above. As we will see, in most cases the RS model does an excellent job of predicting the experimental behavior, both the character of the phenomena and its quantitative expression.

4.1 Immersion Experiments

For the immersion measurements, one additional element must be added to the results of the Theoretical Section and Eqs. (10) through (17). This is the transducer voltage calculation mentioned earlier [27]. The result of that prior analysis, including three-dimensional transducer effects of both transmitter and receiver and realistic beam directivity functions is

$$V(x_i, f) = \frac{ik_f}{4\pi^2} \int_0^{2\pi} d\phi \int_0^{\pi/2-i\infty} \widehat{R}(\theta, f) D_T(\theta, \phi) D_R(\theta, \phi) \sin\theta \, d\theta, \tag{18}$$

where $D_R(\theta, \phi)$ and $D_T(\theta, \phi)$ are the receiver and transmitter directivity functions, respectively, and contain the dependence on x_i, the relative transducer position. Here, k_f is the incident wavevector in the fluid, f is the frequency, $R(\theta, f)$ is the reflection coefficient (for a RS plate), and θ and ϕ are the polar and azimuthal angles. For simplicity we have omitted the explicit dependence of the transducers on frequency and several other constant prefactors before the integrals in Eq. (18). The integral is expressed in terms of angles instead of wavenumbers to emphasize the 3-D nature of the calculation. Substituting for the directivity functions D_T and D_R of the transducers yields an expression which can be integrated numerically to give the receiver voltage for any experimental conditions. Alternatively, the integral in Eq. (18) can be reduced analytically by uniform asymptotics [28]. In order to isolate the effects of roughness and provide the basis of a reliable NDE method, it is essential to eliminate all geometric influences on the signal, such as those arising from diffraction and transducer placement. Equation (18) allows us to do this, and all subsequent immersion results have been calculated by incorporating the rough-surface reflection coefficient into the above integral expression, or into its asymptotic analytical form.

We begin with a series of plots for roughness on the lower plate surface, where the incident angle is fixed at 20° and the transducer separation x_i (see Fig. 8) is incremented in each plot. In each case, the upper frame shows the theoretical prediction, and the lower frame shows the corresponding experimental data. Furthermore, the solid curve denotes the smooth surface, the dashed curve is the 13 μm rms surface, and the dotted curve is the 26 μm rms surface, *in all subsequent plots* in this report. In Fig. 10 is the reflected voltage amplitude for incidence at 20°and a transducer separation x_i of -10 mm. In this case we would expect little or no effect of the roughness, since the receiver is "looking past" the transmitter. From the data and prediction, this supposition is essentially correct. Then, the curve we do observe is largely the effect of diffraction on the received voltage.

At the same conditions, but for $x_i = 0$ mm in Fig. 11 there is still very little effect of the roughness. At this separation the transducer central rays just intersect at the plate surface. This observation squares perfectly with the analysis presented above in conjunction with the reflection coefficient discussion. Simple reflection measurements cannot probe subtle hidden surface roughness with high sensitivity. The prediction is in good agreement with the data, providing confidence in the accuracy of the voltage model.

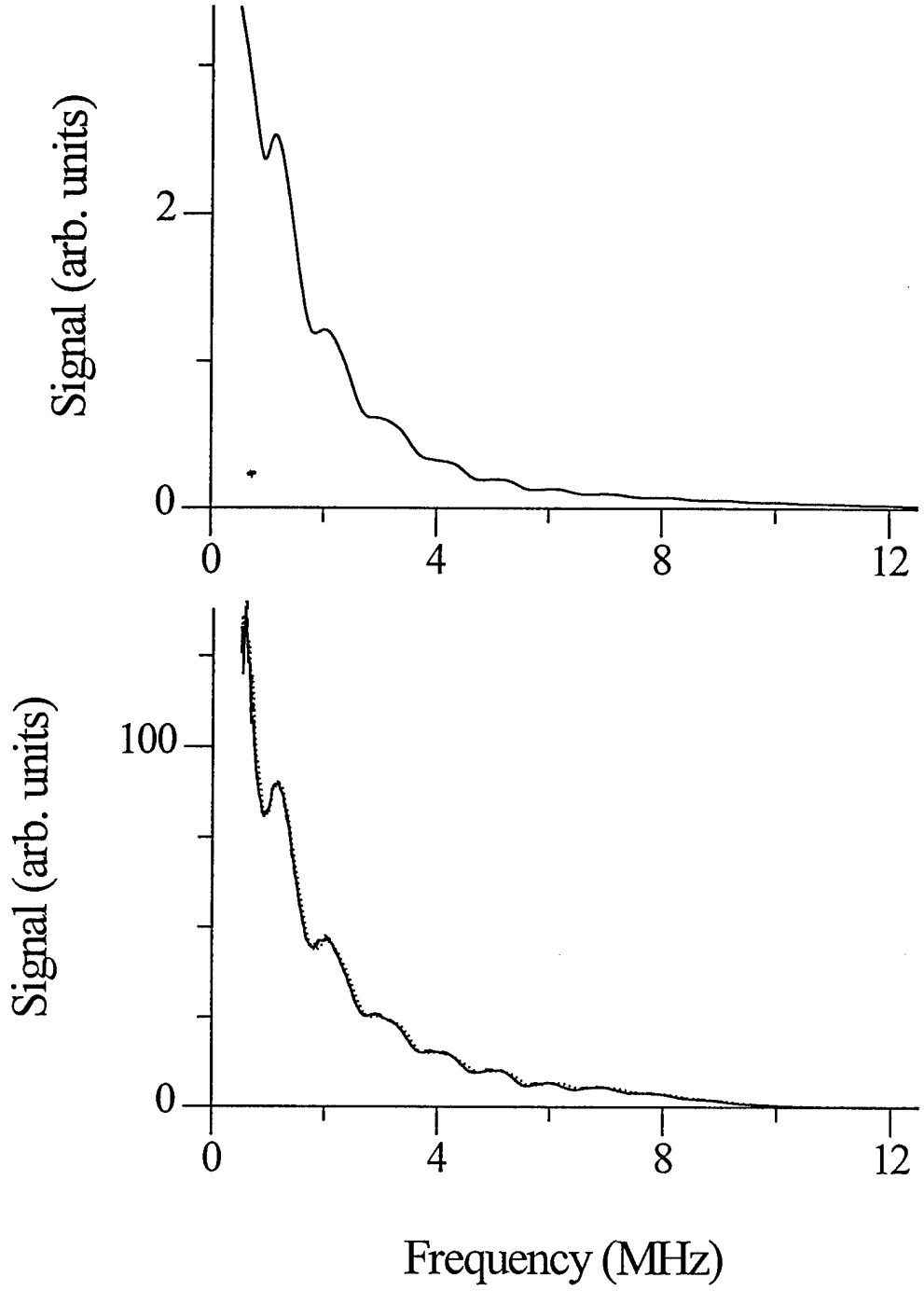

Figure 10: Theoretical and experimental frequency dependence of receiver voltage for smooth (solid) and lower rough surfaces with $h = 13$ μm (dashed) and $h = 26$ μm (dotted), with x_i=-10 mm, and incidence at 20°.

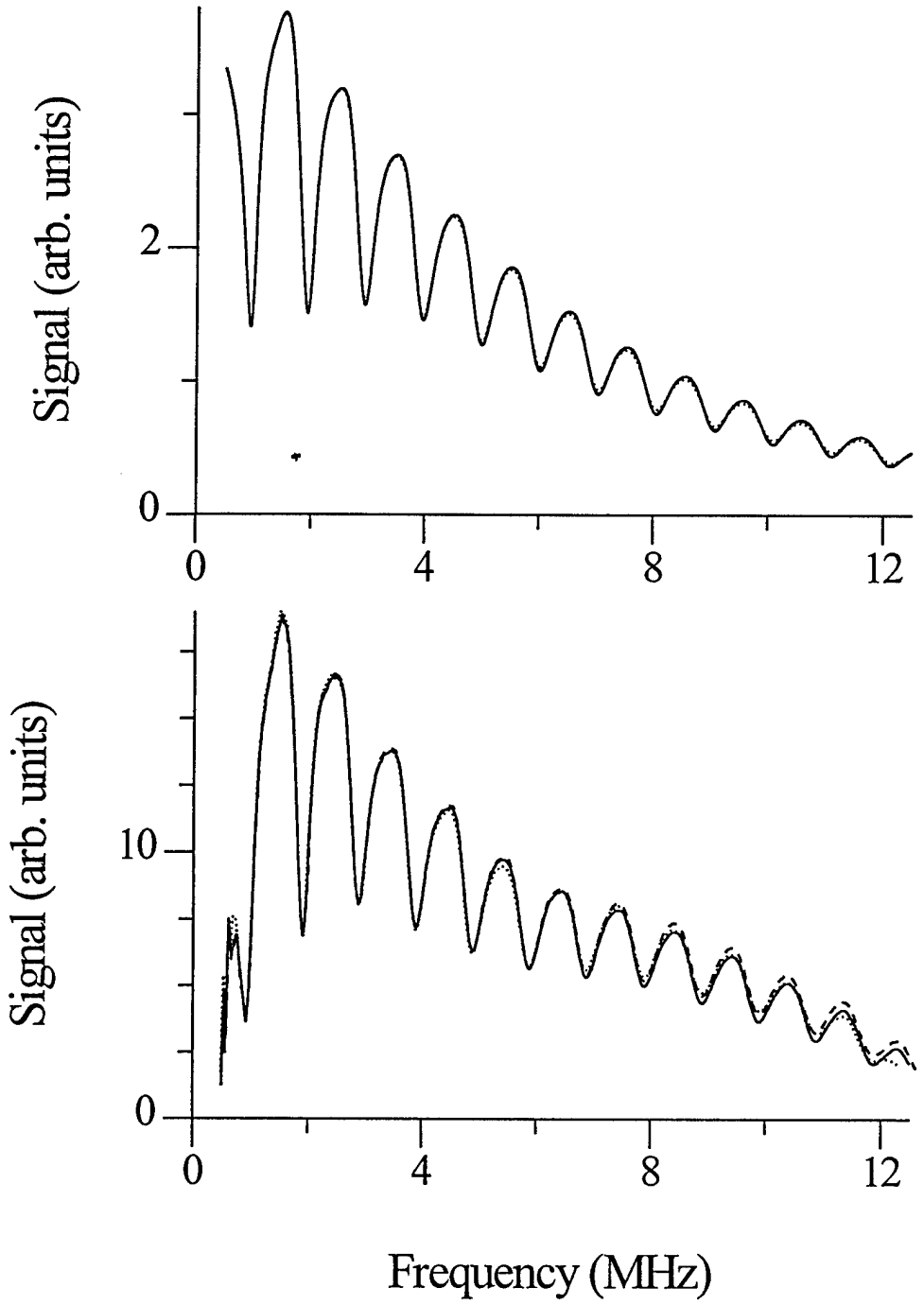

Figure 11: Theoretical and experimental frequency dependence of receiver voltage for smooth (solid) and lower rough surfaces with $h = 13$ μm (dashed) and $h = 26$ μm (dotted), with $x_i = 0$ mm, and incidence at 20°.

At $x_i = 5$ mm in Fig. 12 a small amount of influence of the roughness is apparent, particularly at higher frequency. The data are well modeled by the theory. With $x_i = 10$ mm, shown in Fig. 13, the effect is much stronger, and here the character of the reflection curve changes above about 3 MHz. The change in shape is the result of diffraction effects on the beam. As the beams are separated and the frequency increases, the receiver intercepts less and less energy from the specular component. Consequently, the guided wave minima transform into maxima, as can be seen above about 8 MHz. Again, the model is in very good agreement with the data.

For $x_i = 20$ mm, in Fig. 14, the spectrum is dominated by the leaky guided waves, and the influence of the roughness is pronounced. The series ends with $x_i = 30$ mm in Fig. 15, where the rough surface is a major effect on the reflected voltage. For the 26-μm rms roughness, the signal finally disappears into the noise beyond about 8 MHz. This result is far different from the one near the beginning of this series for $x_i = 0$ mm, where almost no influence could be observed. This contrast demonstrates conclusively the importance and value of probing for hidden roughness (corrosion) in plate-like structures using guided wave behavior.

It should be noted that in the calculations for preceding plots there are no adjustable parameters, only the geometrical variables and the rms roughness height h. However, since the samples we are working with have been sectioned from a larger piece of material, we have found it is occasionally necessary to assume a slightly different ($\sim 5 - -10\%$) rms roughness to achieve a perfect comparison with the data. In this report however, we have made **no** attempt to perfect the comparisons. Therefore, all comparisons reported here for the sandblasted plates have been calculated with the 13-μm or 26-μm estimates. Nonetheless, the reason for such a variation is likely genuine. In the schematic shown in Fig. 8, the only transducer rays that makes a significant contribution to the voltage are contained in the plane of incidence. Therefore, although the beam path is 9 mm or more wide, we sample only rays traveling parallel to the transducer axis. This situation leads to a more restricted sampling than the profilometry used to infer the rms roughness independently from our measurements. It is not too surprising that we may observe fluctuations of 10% or so from the mean. It is our conjecture that such fluctuations account almost entirely for any differences between the model prediction and the experimental data.

To illustrate the differences in the received voltage between top and bottom plate roughness, we present a limited number of plots selected from the data on hand. In Fig. 16, the wave is incident at 20°, and the transducer separation parameter x_i is 0 mm. The frequency spectrum has a much different appearance from the corresponding plot in Fig. 11, with roughness on the bottom surface. Here, each of the three curves is widely separated, and the effect of the roughness is very pronounced. The difference is, of course, that the specular wave component is being strongly attenuated by the roughness, and as the frequency increases, less of this component appears in the voltage. The guided wave signal is small throughout the spectrum, since the transducer separation is so small. In the upper

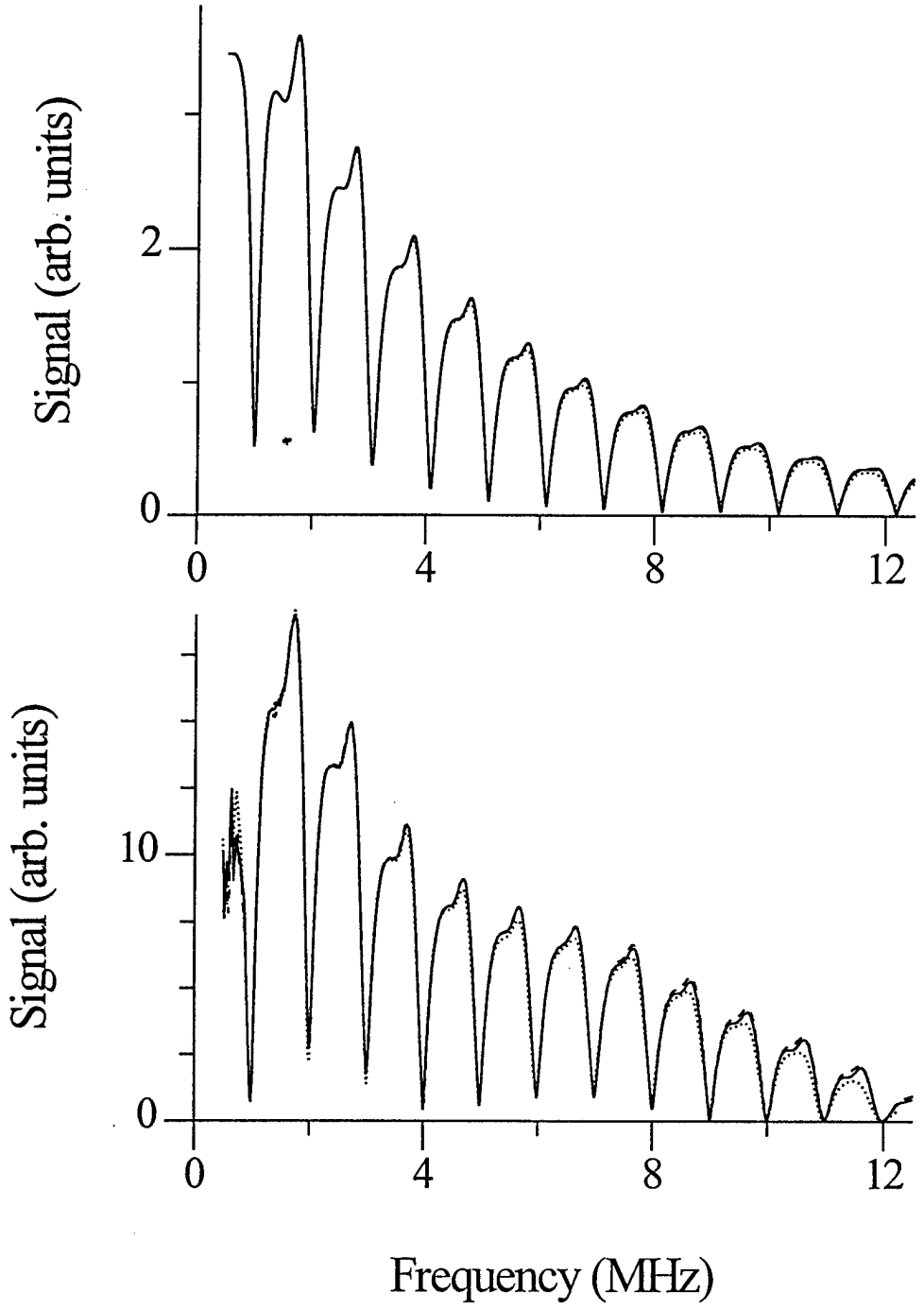

Figure 12: Theoretical and experimental frequency dependence of receiver voltage for smooth (solid) and lower rough surfaces with $h = 13$ μm (dashed) and $h = 26$ μm (dotted), with $x_i = 5$ mm, and incidence at 20°.

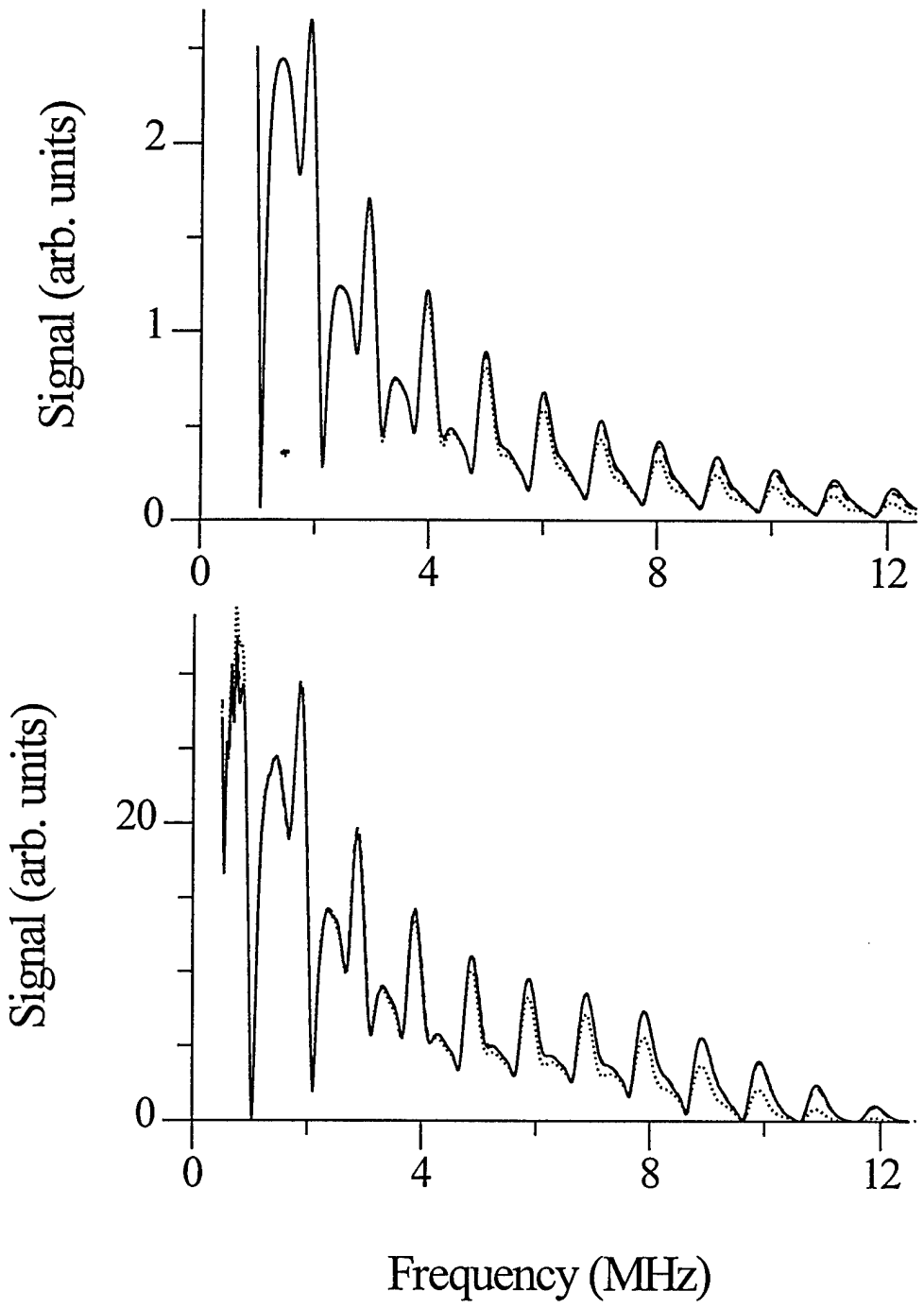

Figure 13: Theoretical and experimental frequency dependence of receiver voltage for smooth (solid) and lower rough surfaces with $h = 13$ μm (dashed) and $h = 26$ μm (dotted), with $x_i = 10$ mm, and incidence at 20°.

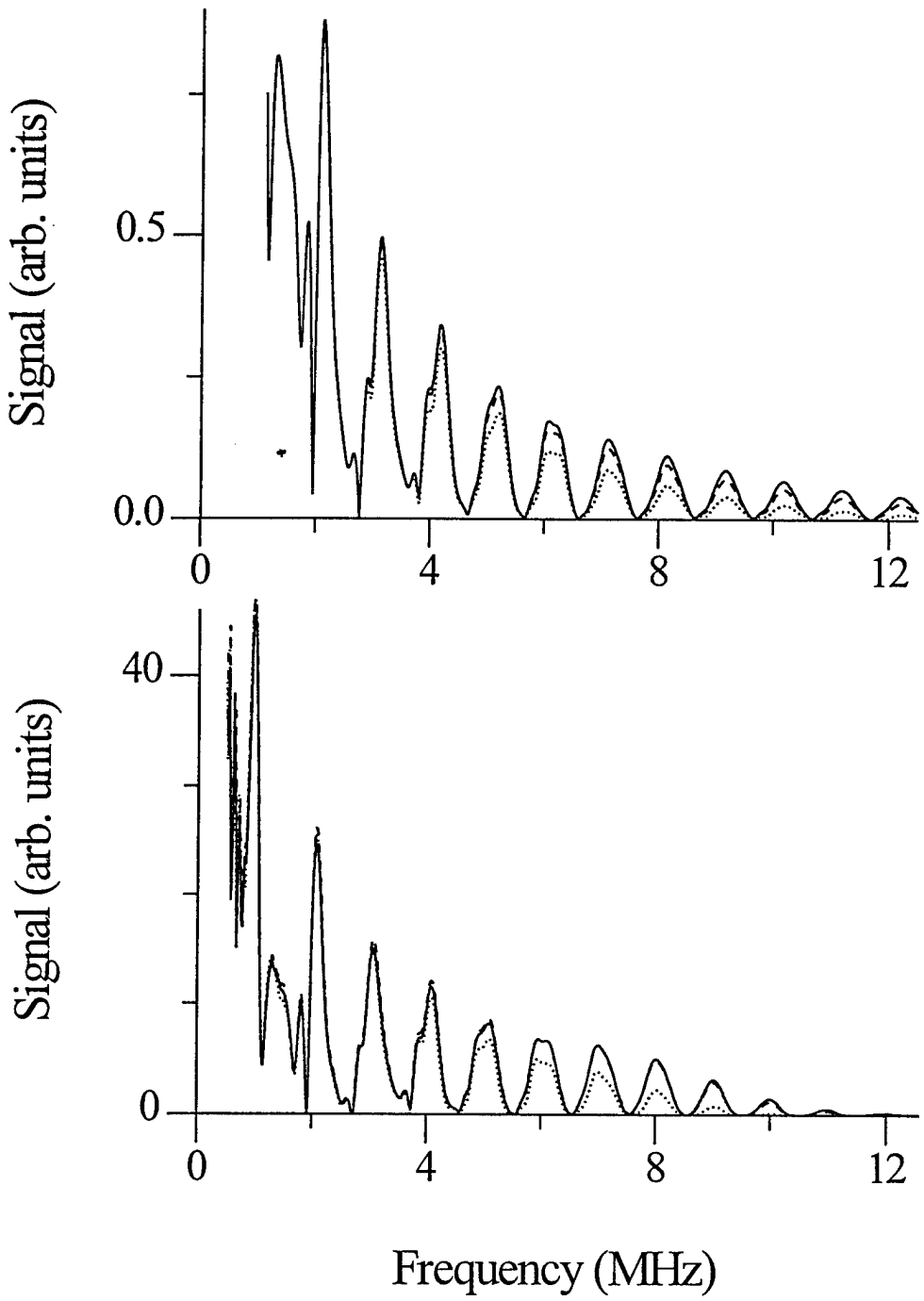

Figure 14: Theoretical and experimental frequency dependence of receiver voltage for smooth (solid) and lower rough surfaces with $h = 13$ μm (dashed) and $h = 26$ μm (dotted), with $x_i = 20$ mm, and incidence at 20°.

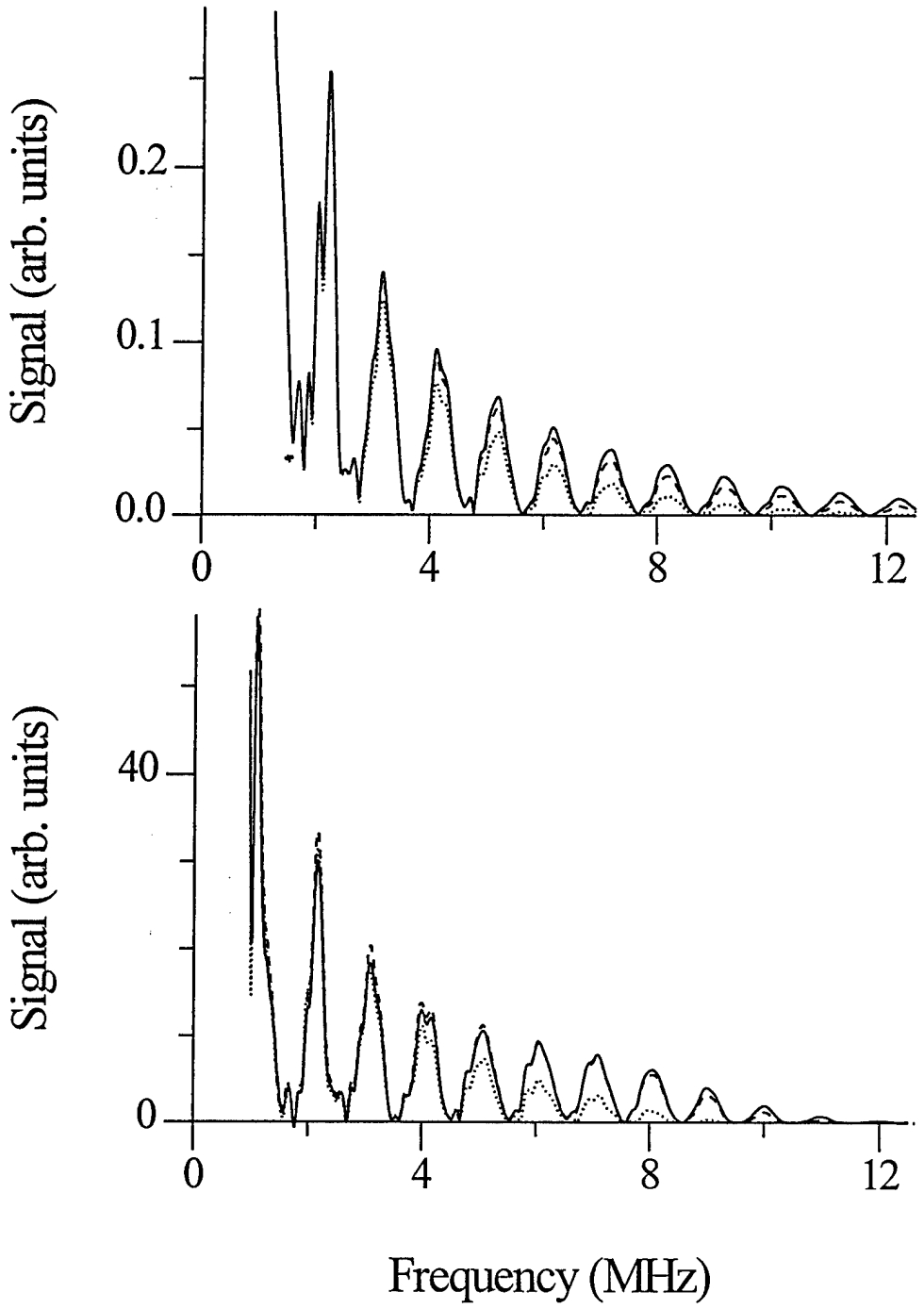

Figure 15: Theoretical and experimental frequency dependence of receiver voltage for smooth (solid) and lower rough surfaces with $h = 13$ μm (dashed) and $h = 26$ μm (dotted), with $x_i = 30$ mm, and incidence at 20°.

frame the model prediction is quite close to the experimental data shown beneath. Here, the details are dominated by diffraction and geometry. The other feature to note is that the small difference in plate thickness from smooth to 26-μm rms roughness has meant that the frequency must be normalized to obtain equivalent behavior from one plate to the next. This procedure is applied for every data set. It would have been perhaps more accurate to plot the spectrum as a function of fd, but the differences are corrected through frequency scaling are never larger than 2%.

For x_i = 10 mm in Fig. 17 the reversion of the guided modes from minima to maxima can be seen again near 3 MHz. Above 5 MHz all guided waves produce maxima in the received voltage, since the receiving transducer is well away from the geometrical reflection of the incident beam. The theoretical calculation shows the familiar close agreement and indicates again the value of guided wave assessment of roughness. Beyond x_i = 10 mm the influence of the specular wave component is nearly gone, and the set of curves for top roughness is essentially identical to that presented earlier for bottom roughness, as for example in Fig. 13.

A different circumstance is met with when the incident angle onto the aluminum plate is 10°. At this angle, unlike 20°, there are several modes very close in frequency. These give rise to some interference that can be seen in the spectra, making this a useful test case for the model. By contrast at 20° the modes are widely separated in frequency, and the influence of one mode on another is negligible. We begin with roughness on the lower plate surface in the 2.3-mm thick plate where x_i = 0 mm, shown in Fig. 18. Here, as before, we show only data at selected values x_i, which are sufficient to illustrate our point. As expected, the effect of roughness for the directly reflected ray is negligible, but the regularly spaced variations in the received voltage spectra, observed at 20°, are not present here. This is the effect of mode interaction in the spatial bandwidth of the transducers. Larger transducer diameters would reduce this effect by concentrating acoustic energy in a narrower range of angles about the transducer central ray.

In Fig. 19 for x_i = 10 mm the transition to mostly guided wave signal contributions occurs near 4 MHz, yet the complicated structure (more so than at 20°) is the result of modes in close proximity. The model calculation demonstrates the importance of accounting properly for the diffraction effects. Most of the unusual signal excursions are in fact predictable consequences of mode interaction and experimental geometry. This point is made even better in the data presented for x_i = 30 mm in Fig. 20. Rapid signal variations at the peaks occurring above 4 MHz are reproduced almost exactly by the model prediction. These, once again, are principally the result of mode interaction in the transducer spatial bandwidth.

Behavior suggestive of the series at α = 20° for top surface roughness presented earlier in Figs. 16 and 17 can be seen here as well for an incident angle of α = 10°. At x_i=0 mm in Fig. 21 the three curves for smooth, small roughness, and large roughness become more widely separated with increasing frequency as the roughness interferes with the

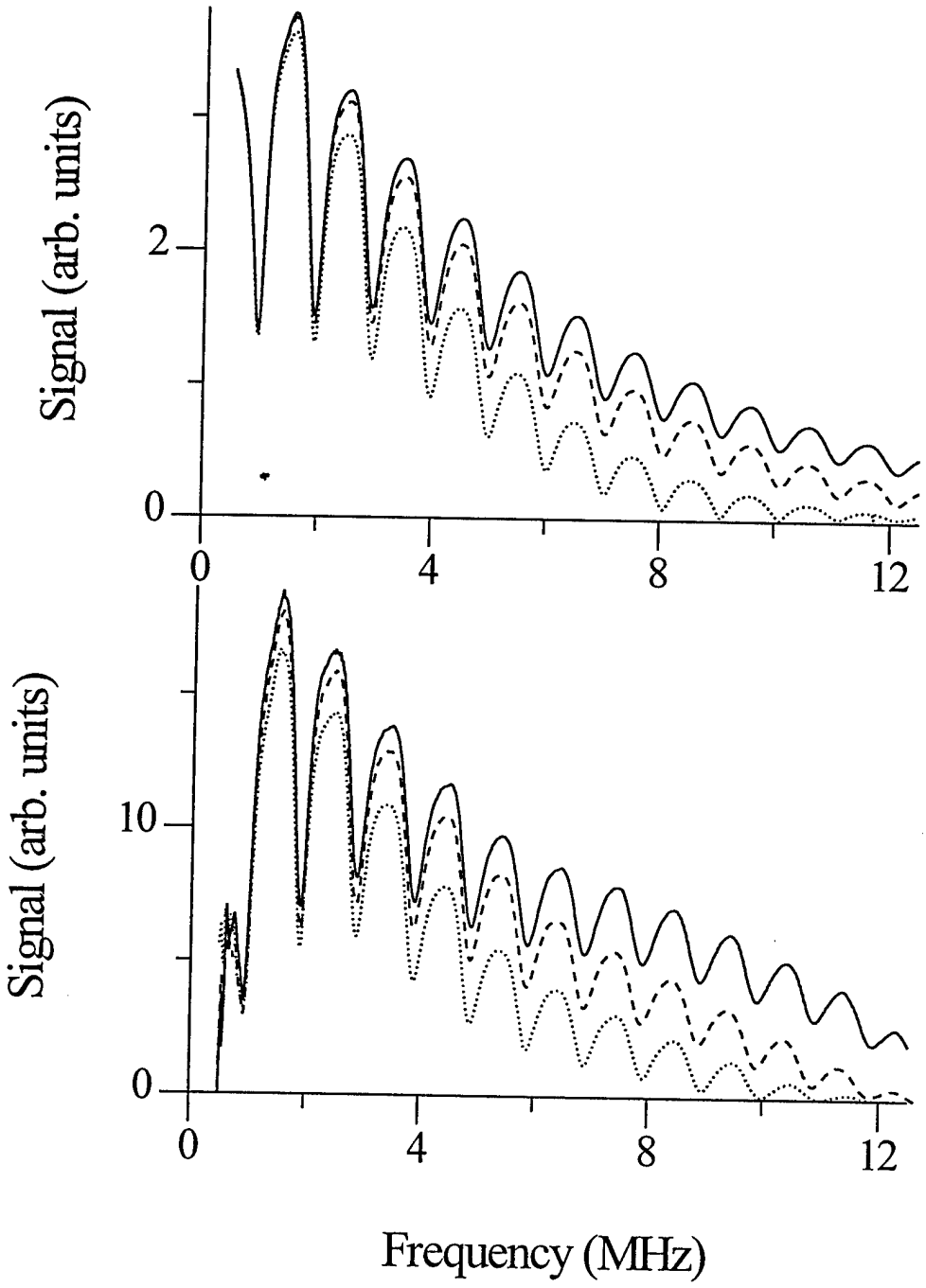

Figure 16: Theoretical and experimental frequency dependence of receiver voltage for smooth (solid) and upper rough surfaces with $h = 13$ μm (dashed) and $h = 26$ μm (dotted), with $x_i = 0$ mm, and incidence at 20°.

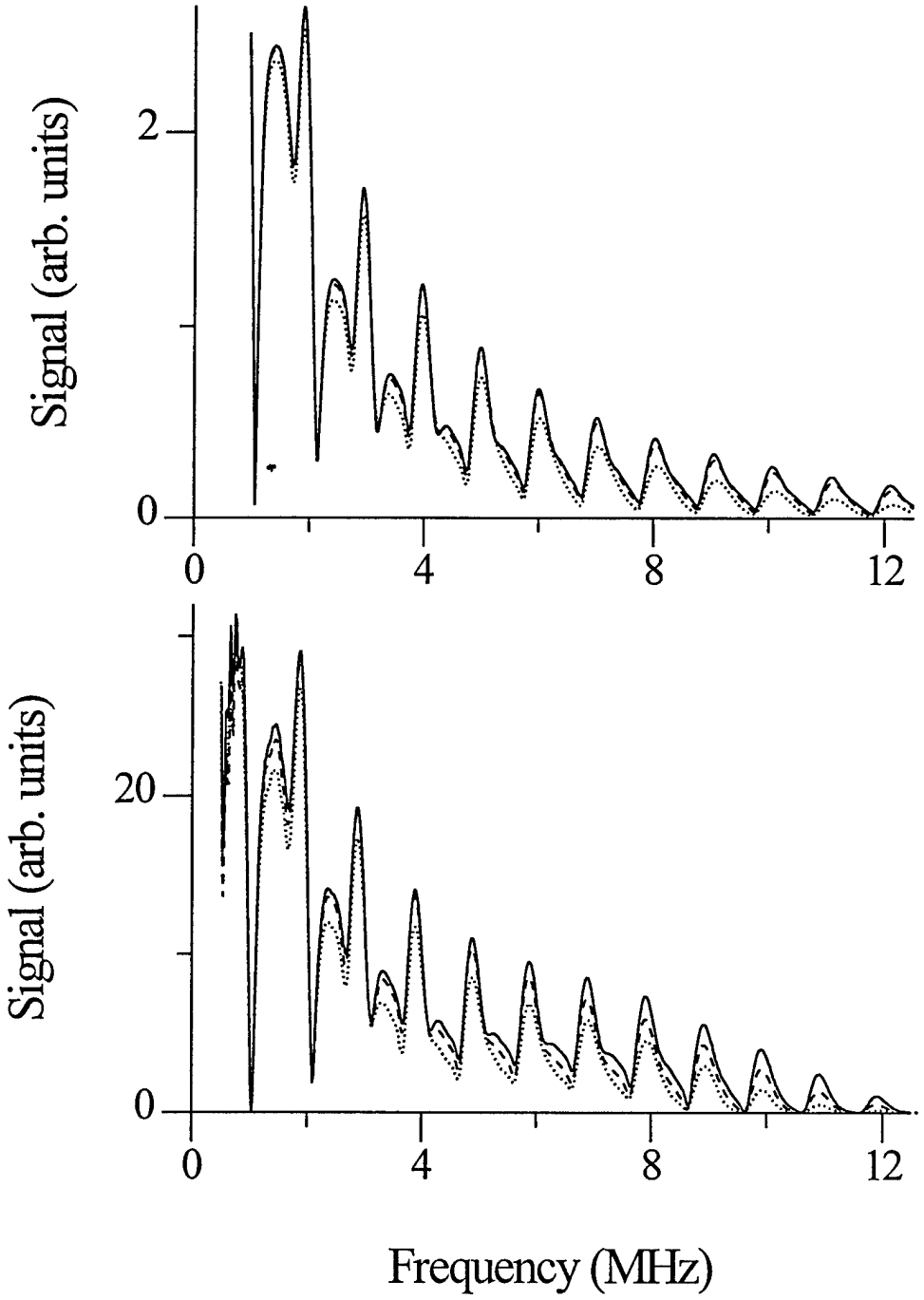

Figure 17: Theoretical and experimental frequency dependence of receiver voltage for smooth (solid) and upper rough surfaces with $h = 13$ μm (dashed) and $h = 26$ μm (dotted), with $x_i = 10$ mm, and incidence at 20°.

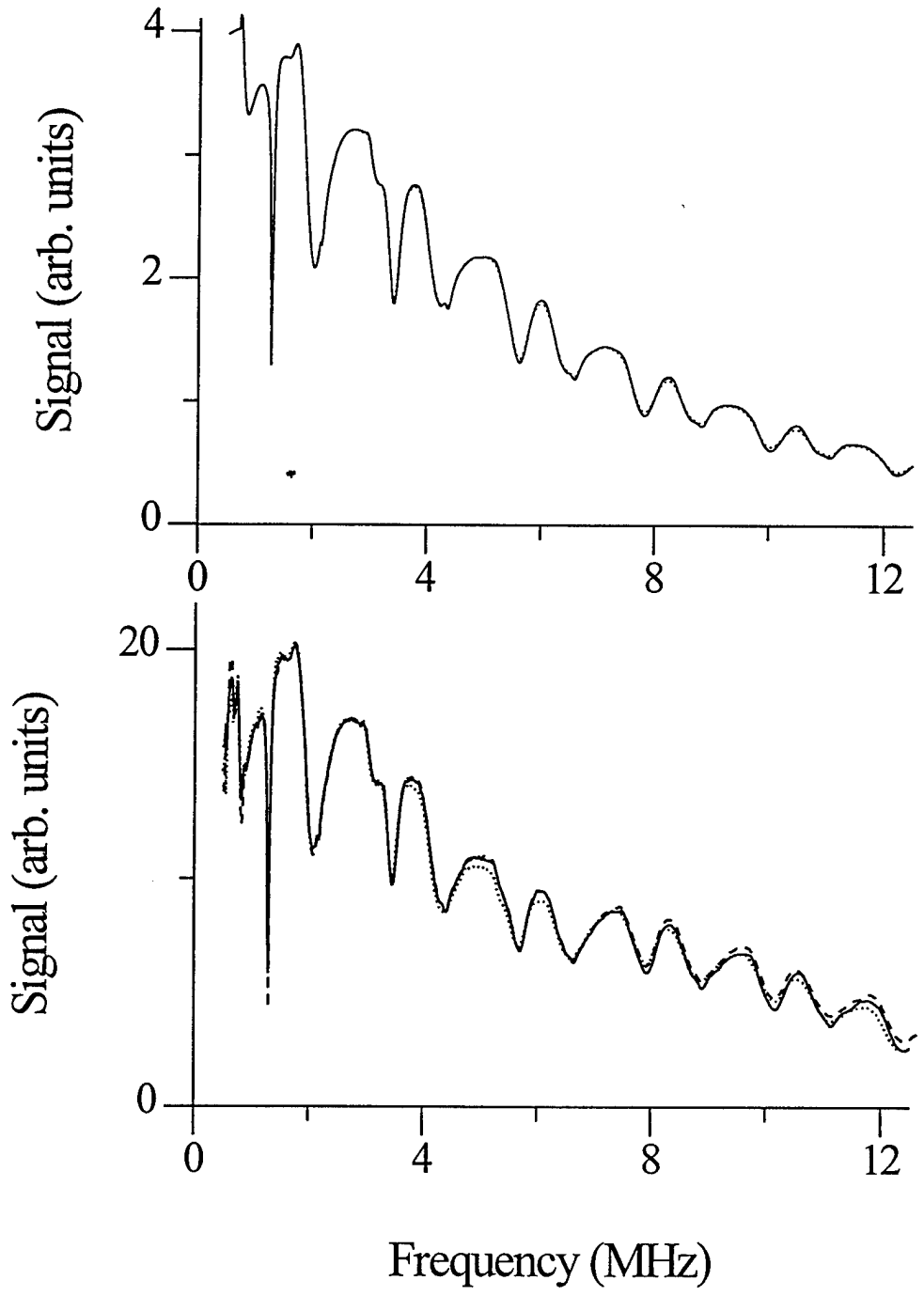

Figure 18: Theoretical and experimental frequency dependence of receiver voltage for smooth (solid) and lower rough surfaces with $h = 13$ μm (dashed) and $h = 26$ μm (dotted), with $x_i = 0$ mm, and incidence at 10°.

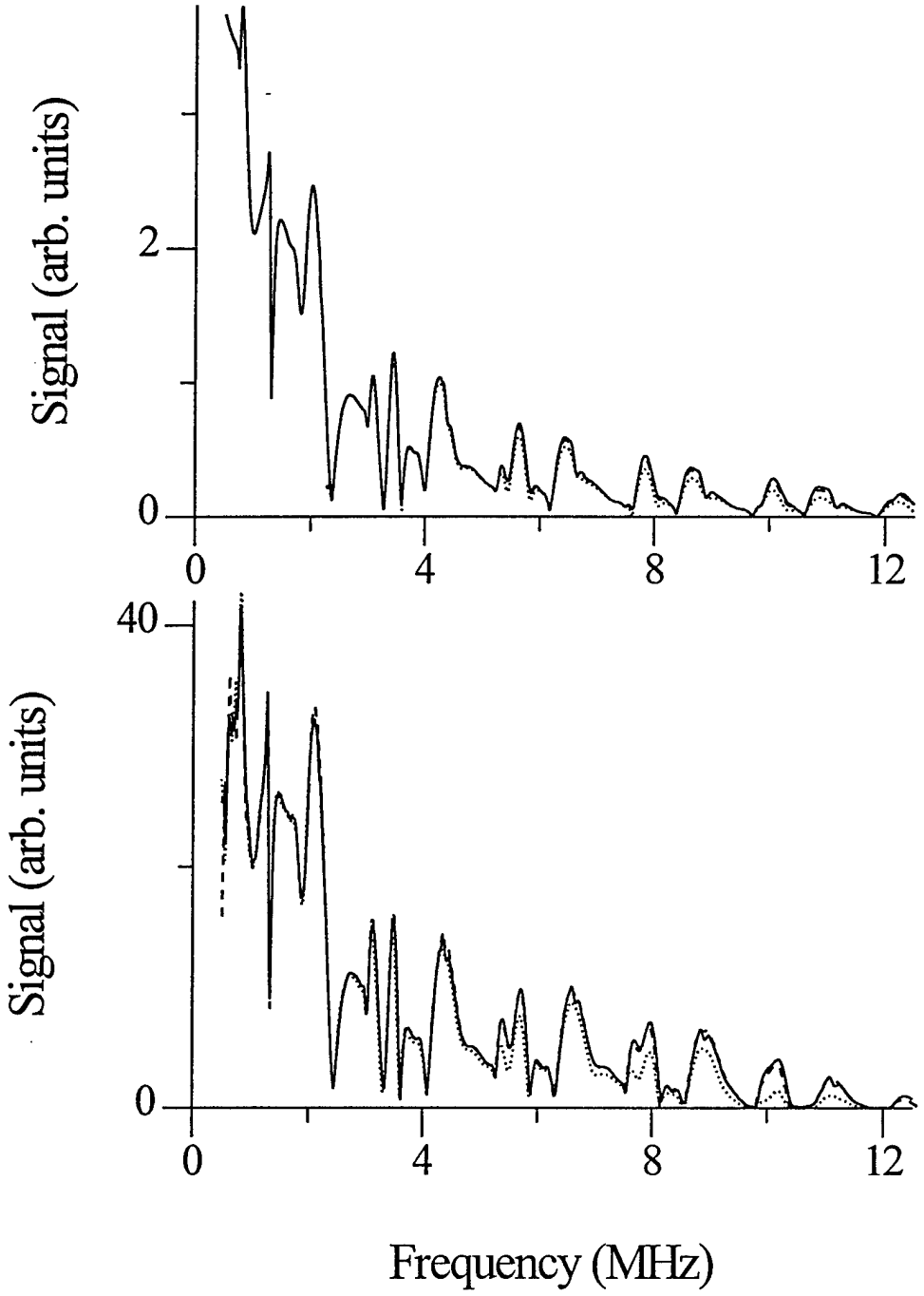

Figure 19: Theoretical and experimental frequency dependence of receiver voltage for smooth (solid) and lower rough surfaces with $h = 13$ μm (dashed) and $h = 26$ μm (dotted), with $x_i = 10$ mm, and incidence at 10°.

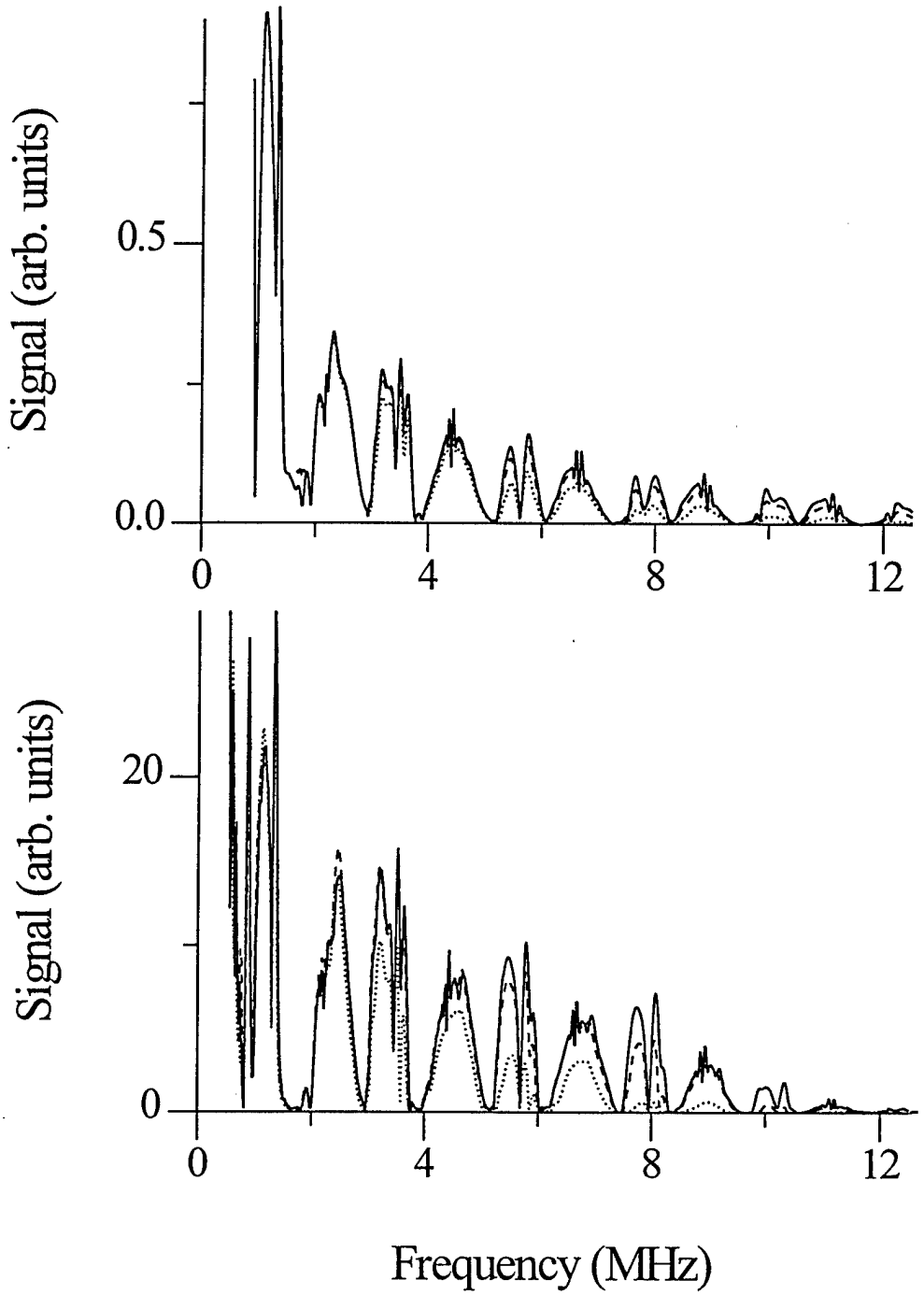

Figure 20: Theoretical and experimental frequency dependence of receiver voltage for smooth (solid) and lower rough surfaces with $h = 13$ μm (dashed) and $h = 26$ μm (dotted), with $x_i = 30$ mm, and incidence at 10°.

specular reflection component. As before, the irregularity in the spectra is the consequence of mode interactions. In Fig. 22 with x_i=10 mm the complicated spectral behavior is still pronounced, but with much less overlap between transmitter and receiver footprints (especially above 4 or 5 MHz), the difference between this plot and that in Fig. 19 is not so large.

These differences vanish entirely for the data at x_i=30 mm in Fig. 23 which are virtually identical to those in Fig. 20. Once out of the way of the specular component (the one that is strongly affected by roughness), the guided damping takes over, and it makes almost no difference in the reradiated signal whether the guided wave is damped by a rough upper surface or by a rough lower surface. There is, however, one small difference in that the wave must leak *through* the upper rough surface, and at this point the roughness gets one last chance to dephase the wave before it reaches the receiver. While this effect is not large, its influence can be seen especially in the mode peak near 7 MHz in both experiment and prediction in Figs. 20 and 23. The amplitude of either the 13-μm or 26-μm rms roughness curve is smaller for top surface roughness in Fig. 23.

In addition to the spectral plots presented in the preceding pages, we have also made extensive studies of reflected amplitude as a function of coordinate. Since these data portray essentially the same behavior as the spectral data, but from a different standpoint, and are of somewhat less interest in terms of eventual applications, we present only an abbreviated version of the data collected in these experiments. Figure 24 shows a coordinate scan for the S_5 Lamb wave mode with incidence at 20° and a fixed frequency of 11 MHz. The influence of the rough surface is at once apparent in the progressive reduction of the secondary peak following ($>$ 5 mm) the specular reflection, in which there is no roughness information. The sharp decline in energy at x_i = 5 mm is the result of exact phase cancellation of the remnant specular reflection and the developing leaky guided wave. The guided wave dominates thereafter, and the decreased amplitude in the dashed and dotted curves shows the effect of roughness.

The experimental amplitude of the specular reflection is not exactly predicted by the model for the following reason. These data are acquired by making stepped frequency scans at many values of x_i from -15 mm to 40 mm. Since the plates are not exactly the same thickness, the corresponding mode (in this case S_5) will not occur at exactly the same frequency. But the frequency data is discrete. This fact would not be a problem were it not for the extremely strong dependence of signal on frequency at precisely the occurrence of a mode. (See Fig. 4; the modes occur at the bottom of the sharp minima.) There is nothing of particular significance here, except to note that the specular reflection, what one gets in a conventional pulse-echo or pitch-catch type ultrasonic test, reveals nothing about the roughness. Only the *ratio* of the specular to the guided wave amplitude has significance for deducing parameters related to the roughness.

By way of illustration, similar data are shown in Fig. 25 for the S_3 mode at α = 10° and a fixed frequency of 3.22 MHz. Here, the roughness effect at relatively low frequency

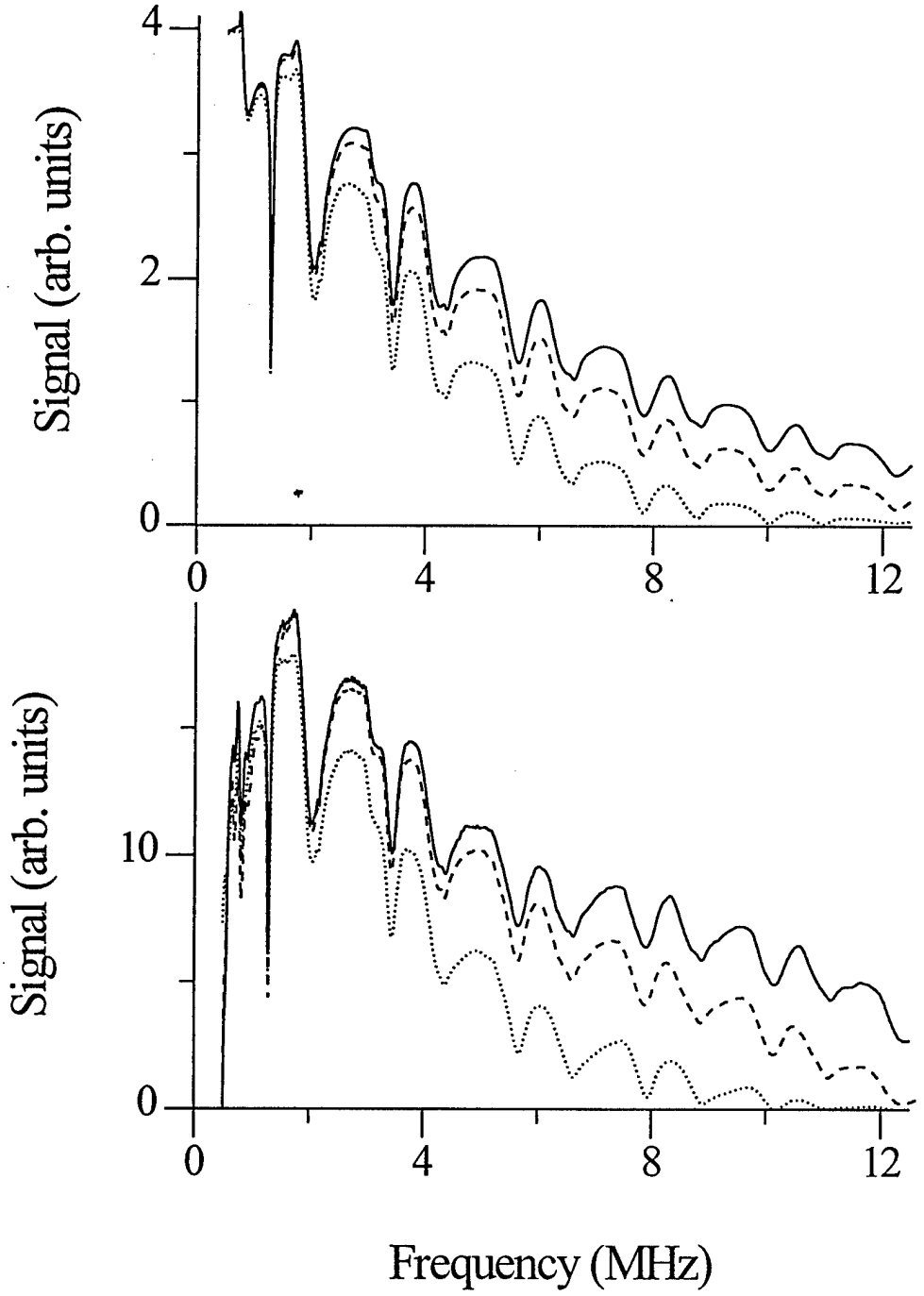

Figure 21: Theoretical and experimental frequency dependence of receiver voltage for smooth (solid) and upper rough surfaces with $h = 13$ μm (dashed) and $h = 26$ μm (dotted), with $x_i = 0$ mm, and incidence at 10°.

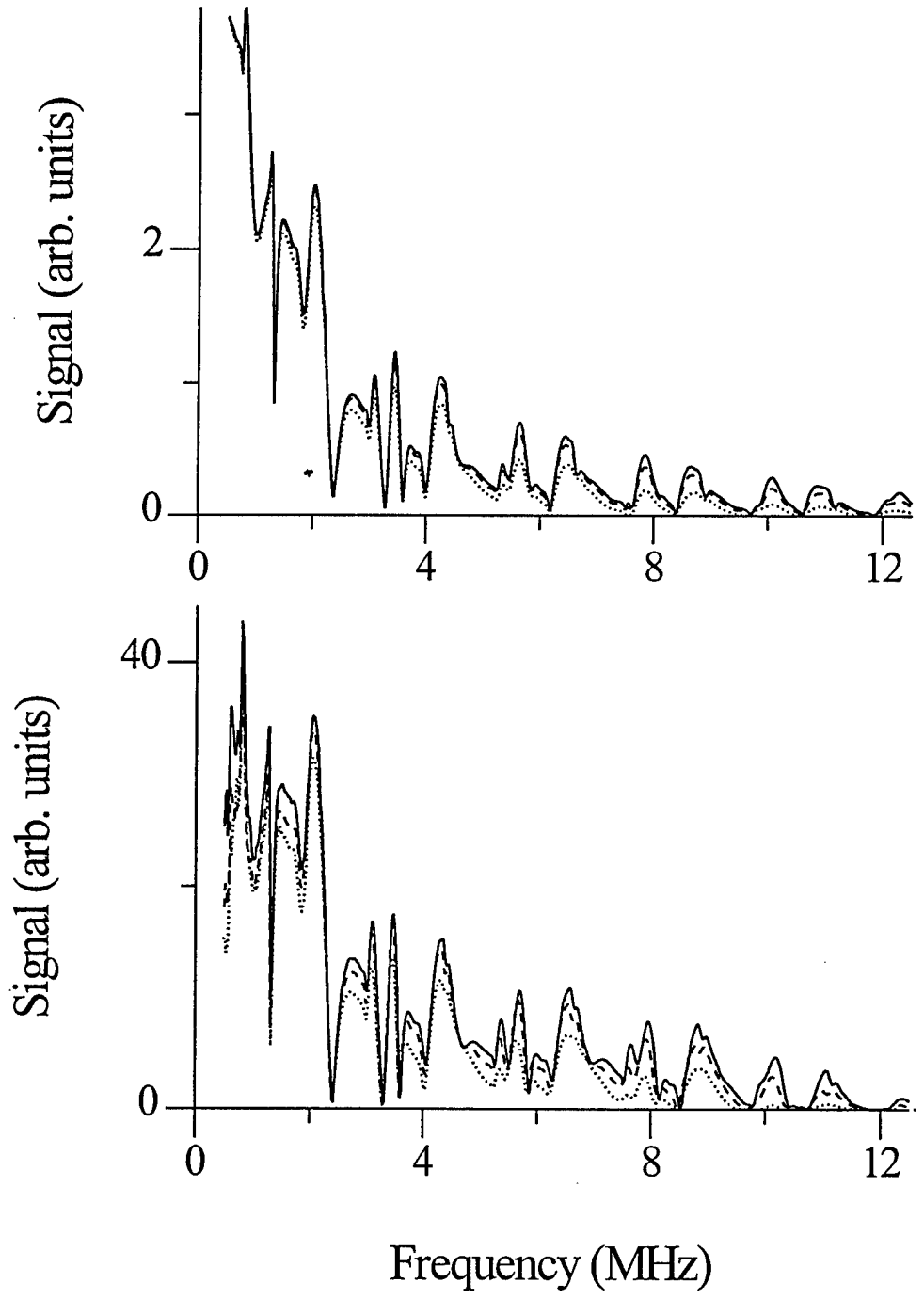

Figure 22: Theoretical and experimental frequency dependence of receiver voltage for smooth (solid) and upper rough surfaces with $h = 13$ μm (dashed) and $h = 26$ μm (dotted), with $x_i = 10$ mm, and incidence at 10°.

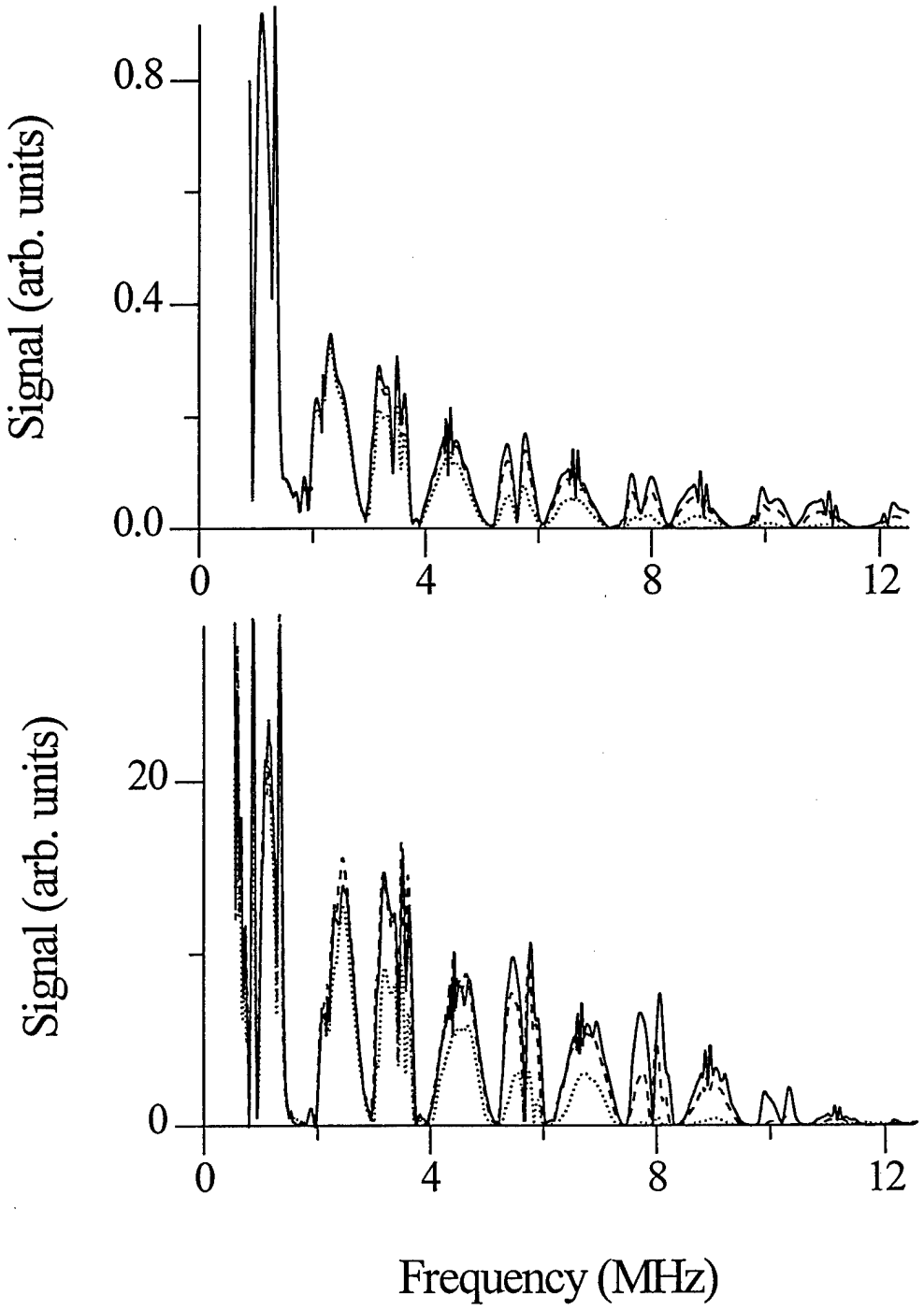

Figure 23: Theoretical and experimental frequency dependence of receiver voltage for smooth (solid) and upper rough surfaces with $h = 13$ μm (dashed) and $h = 26$ μm (dotted), with $x_i = 30$ mm, and incidence at 10°.

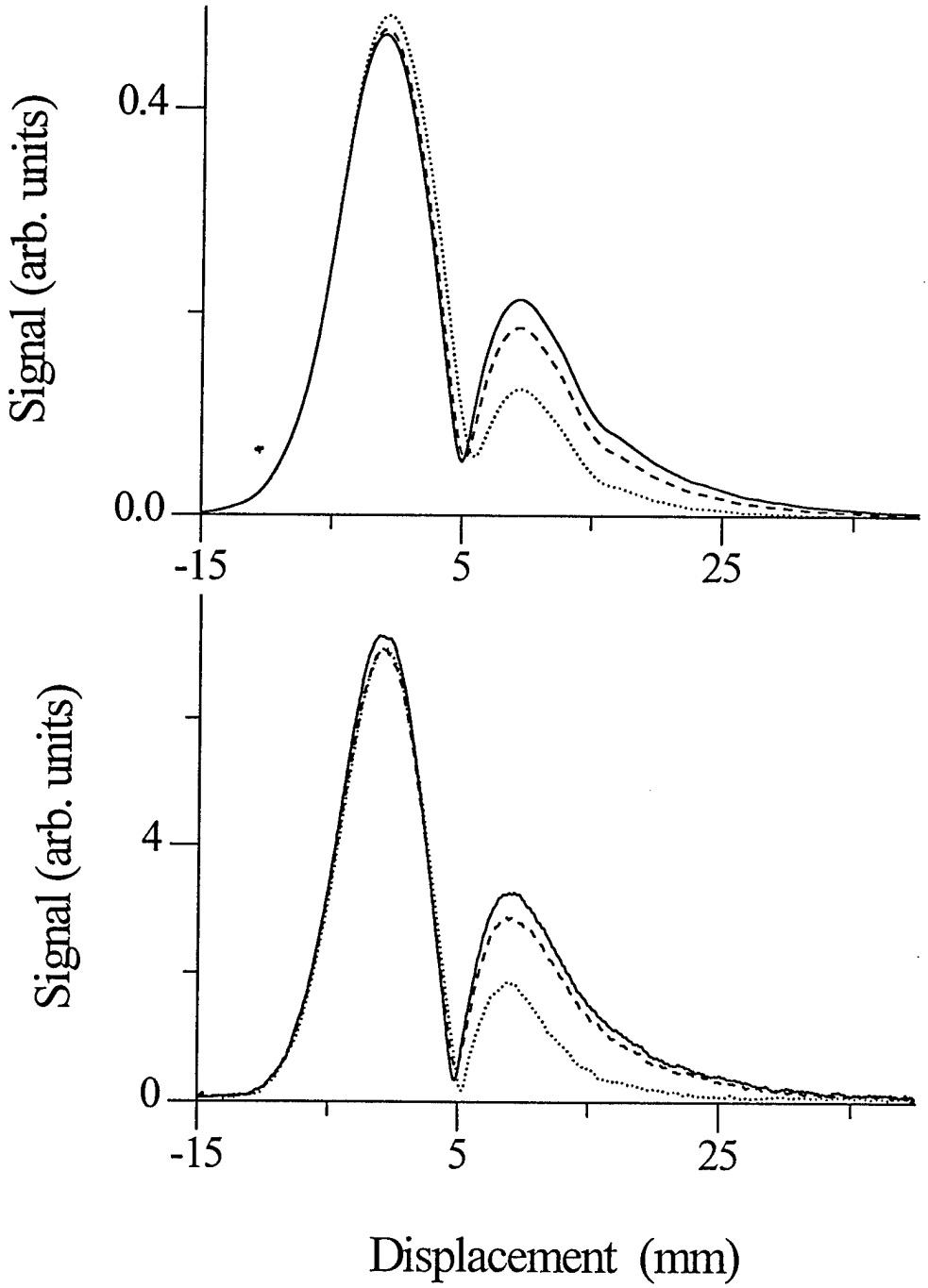

Figure 24: Theoretical and experimental dependence on displacement x_i of receiver voltage for smooth (solid) and upper rough surfaces with $h = 13$ μm (dashed) and $h = 26$ μm (dotted) and incidence at 20° for the S_5 mode at 11 MHz.

is small, even for the 26-μm rms surface. Data acquired at 7.75 MHz for the S_7 mode (likewise at $\alpha = 10°$) shows a greater effect of roughness, as seen in Fig. 26; this result is expected. The predictions are close to the experimental data, with the proviso mentioned earlier concerning the absolute height of the specular peak.

These coordinate scan data complete the presentation of results from immersion testing on smooth and rough aluminum plates. A wide range of phenomena has been explored and important questions have been answered concerning the best choices of inspection parameter values to optimize the effects of a rough surface on the guided wave signal. As well, we have seen that conventional testing methods would be of little use in developing methods to reveal the presence of weak, hidden roughness (corrosion) in plate-like aerospace materials. Immersion has been chosen for extensive experimental concentration because of the reliable transfer of ultrasonic energy between transducer and component under test. In this way the predictions of our newly developed rough surface model could receive the most critical testing to uncover weakness or incompleteness in the model. The excellent performance of the model under virtually every circumstance gives us confidence that it can be eventually applied in an inversion algorithm to deduce roughness from measurements.

4.2 Contact Measurements

Many measurements have been made in contact mode, using polystyrene wedges in place of a couplant fluid. The wedge angles (there are two sets of wedges) have been calculated to produce waves with phase velocities in the aluminum plate centered on 4.7 km/s and 3.2 km/s. Most of the experiments have been performed with the 3.2 km/s wedge (wedge angle = 45°). The notorious difficulty of attaining a reliable, consistent contact in this mode of operation has been a problem in these studies as well. We have attempted to circumvent these difficulties by making measurements at many physical locations and performing appropriate averages to reduce any bias introduced by inconsistent contacts. The major effect of a changing contact is the variation in signal amplitude. There is generally little effect on the shape of the signal spectrum. Since we are principally interested in relative amplitudes within a spectrum, the contact problem is not as severe as it might be for a purely amplitude-based measurement.

Experimental data obtained in this mode are shown in Fig. 27. Here, the result of many measurements performed on different portions of the plate are averaged and presented as signal amplitude versus frequency. The thinner plate (1.4 mm) is shown in the top frame and the thicker one (2.3 mm), having more observable modes, is shown in the bottom. The three different curves in each frame relate to different separations of the transducer axis intersection x_i, as shown schematically in the inset; the three curves are solid ($x_i = 20$ mm), dashed ($x_i = 30$ mm), and dotted ($x_i = 40$ mm). For the thinner sample in the upper frame fewer modes are produced within the transducer bandwidth, but the effect

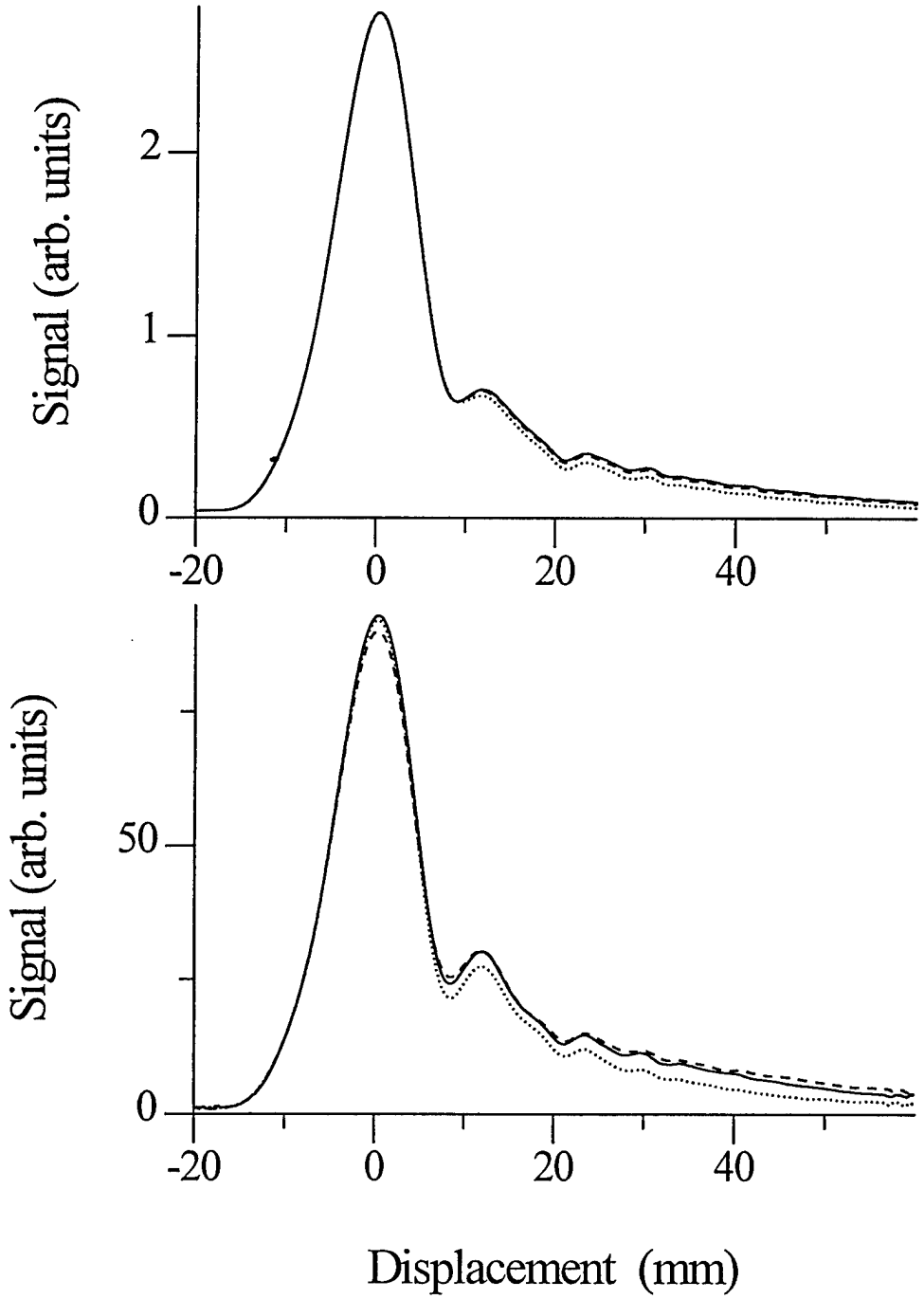

Figure 25: Theoretical and experimental dependence on displacement x_i of receiver voltage for smooth (solid) and upper rough surfaces with $h = 13$ μm (dashed) and $h = 26$ μm (dotted) and incidence at 10° for the S_3 mode at 3.22 MHz.

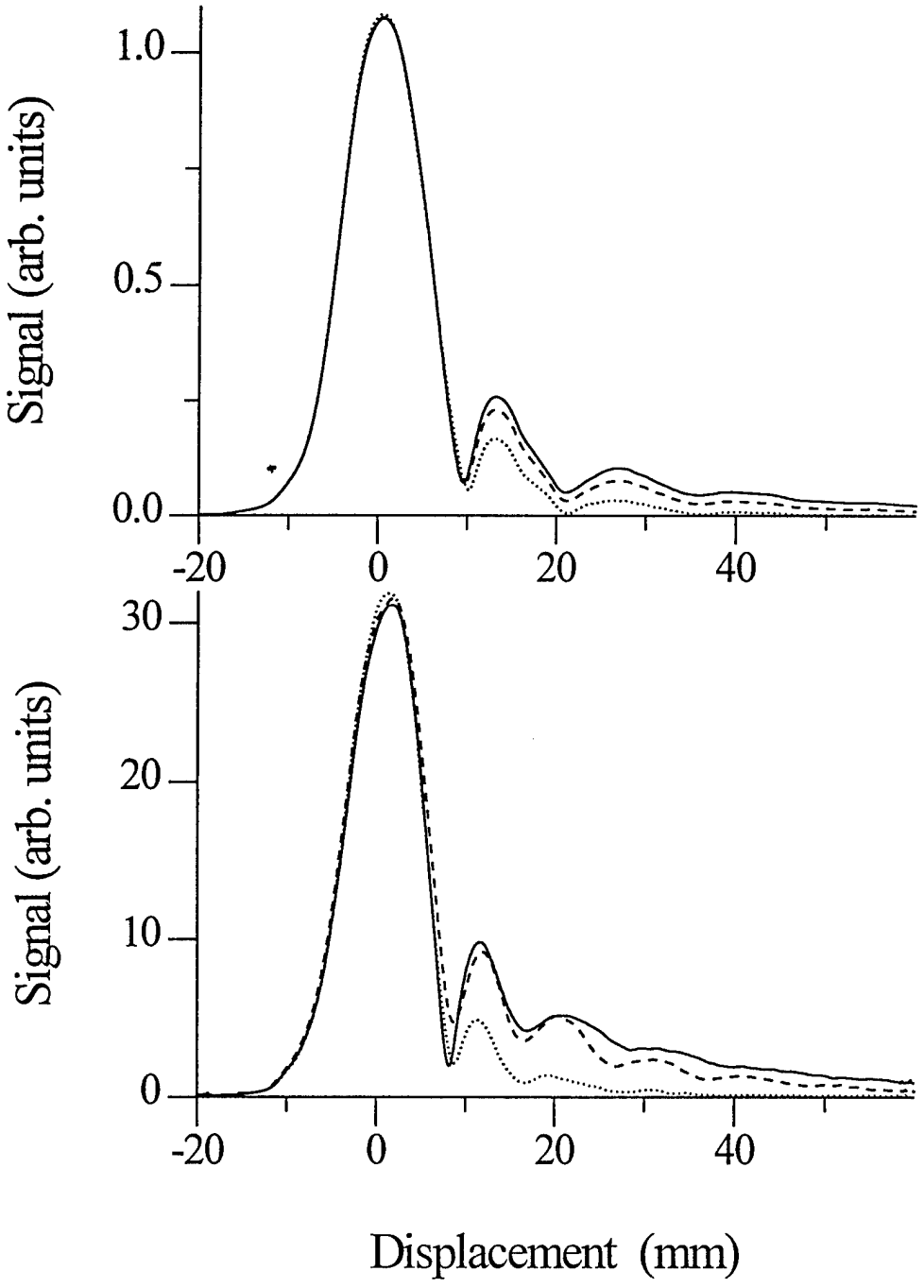

Figure 26: Theoretical and experimental dependence on displacement x_i of receiver voltage for smooth (solid) and upper rough surfaces with $h = 13$ μm (dashed) and $h = 26$ μm (dotted) and incidence at 10° for the S_7 mode at 7.75 MHz.

of increasing separation is more pronounced from mode to mode. The S_0 mode in either case is very little affected since the phase velocity and frequency lie near a minimum in $\mathrm{Im}(\xi)$, as shown for the antisymmetric modes in Fig. 1. In the lower frame more modes are generated in the thick plate showing the progressive effects of both increasing frequency and transducer separation.

To analyze the behavior in Fig. 27 for comparison to our model, these data are accumulated in Fig. 28. In the upper frame are the results for the 13-μm RS plate, while the 26-μm RS plate data and calculations are reported in the lower frame. Each experimental curve is denoted by a different plotting symbol, (+) for the A_3 mode, (▪) for the S_2 mode, and (•) for the A_2 mode, referring to a different mode from Fig. 27. Each mode occurs at a constant frequency determined by the wedge angle, which is fixed for the experiment. Despite difficulties with the contact, the normalized amplitude data falls on, or close to, the expected straight line. The slopes are higher for the 26-μm roughness than for the smaller h. Again, we should expect this behavior. The solid lines through the data in each case are best-fit curves from which attenuation values can be deduced. The theoretical estimates for the slopes are calculated using Eqs. (3) and (4), and we find a ratio between the square roots of the slopes of the experimental curves that is entirely consistent with the roughness ratio of the mode occurrences. The root slope ratio $\mathcal{R}_{x/y}$ is given by

$$\mathcal{R}_{S_1/A_1} = \sqrt{\frac{\mathcal{S}_{S_1}(h)}{\mathcal{S}_{A_1}(h)}}, \quad \text{or} \tag{19}$$

$$\mathcal{R}_{h_1/h_2} = \sqrt{\frac{\mathcal{S}_{A_1}(h_1)}{\mathcal{S}_{A_1}(h_2)}},$$

where $\mathcal{S}_{S_1}$ is the slope of the S_1 mode. For the slopes of the curves in Fig. 28 we calculate a roughness root slope ratio $\mathcal{R}_{h_1/h_2}$ of 2.2, whereas we expect a ratio of 2 (= 26μm/13μm). This comparison is very favorable considering the inconsistencies in the contact, and it demonstrates the relative lack of sensitivity to the disturbing influence of contact variations.

A further result on different specimen is shown in Fig. 29. The indented specimen (h = 44 μm) has a section of roughened surface of different length. The solid curve is for no roughness, and for the dashed curve the guided wave passes through a 12.7-mm region of roughness. The dotted curve is for propagation through a 25.4-mm roughened segment. Each mode peak is also labeled. As the frequency increases with mode index, the damping rapidly attenuates the tone-burst signal.

A different demonstration is shown in Figs. 30 and 31. The indented specimen (h = 60 μm) has a section of roughened surface located either on the top or bottom surface. With contact mode coupling, this distinction should make no difference. And our data show that it does not. The only differences that do appear arise from coupling inconsistencies and one other possible source of systematic error. The indented samples are produced in

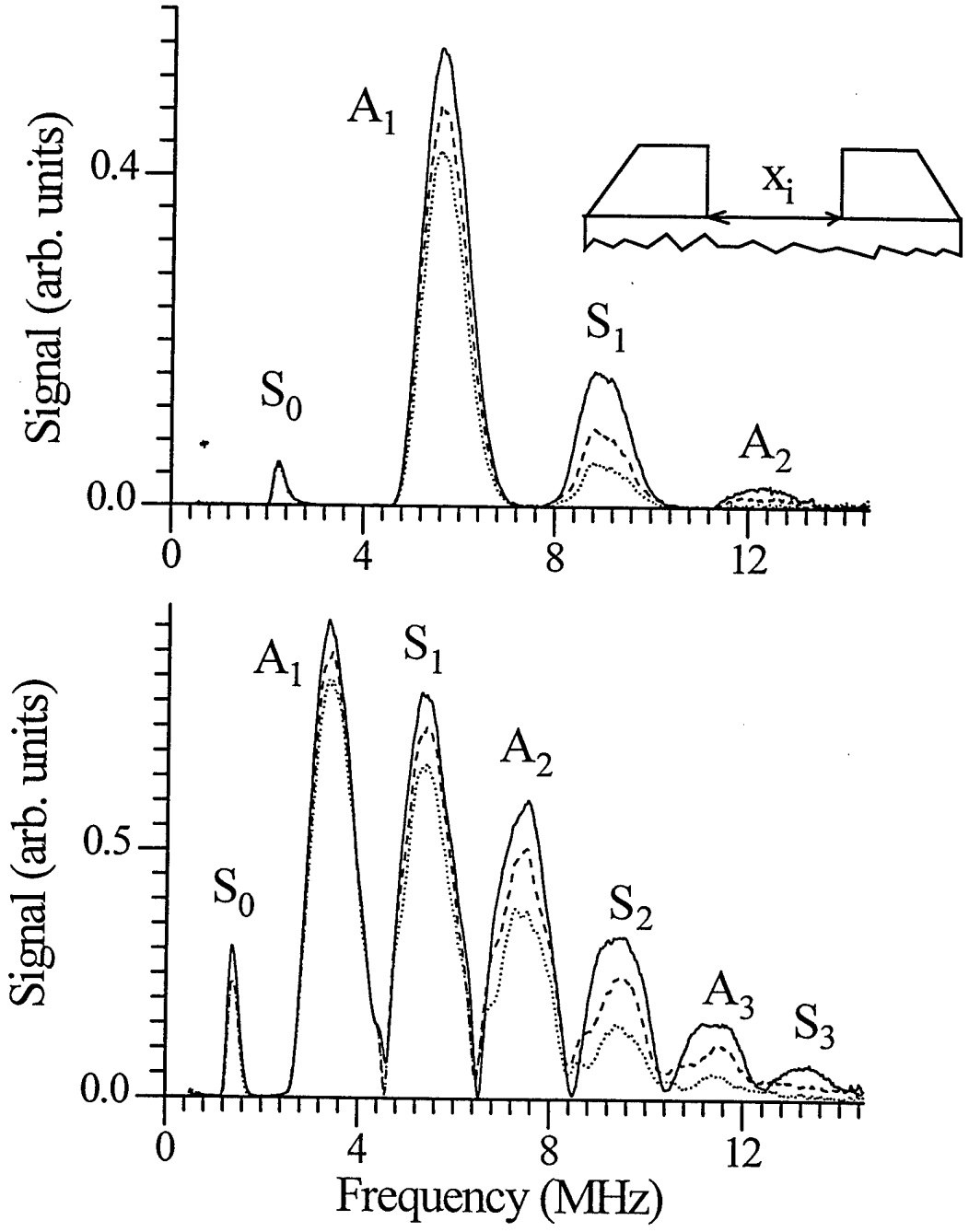

Figure 27: Shoe-contact experimental signal from rough aluminum sandblasted plates ($h = 26$ μm) for three different transducer axis separations x_i (solid: 20 mm; dashed: 30 mm; dotted: 40 mm); top frame is thin plate (1.4 mm) and bottom frame is thick plate (2.3 mm).

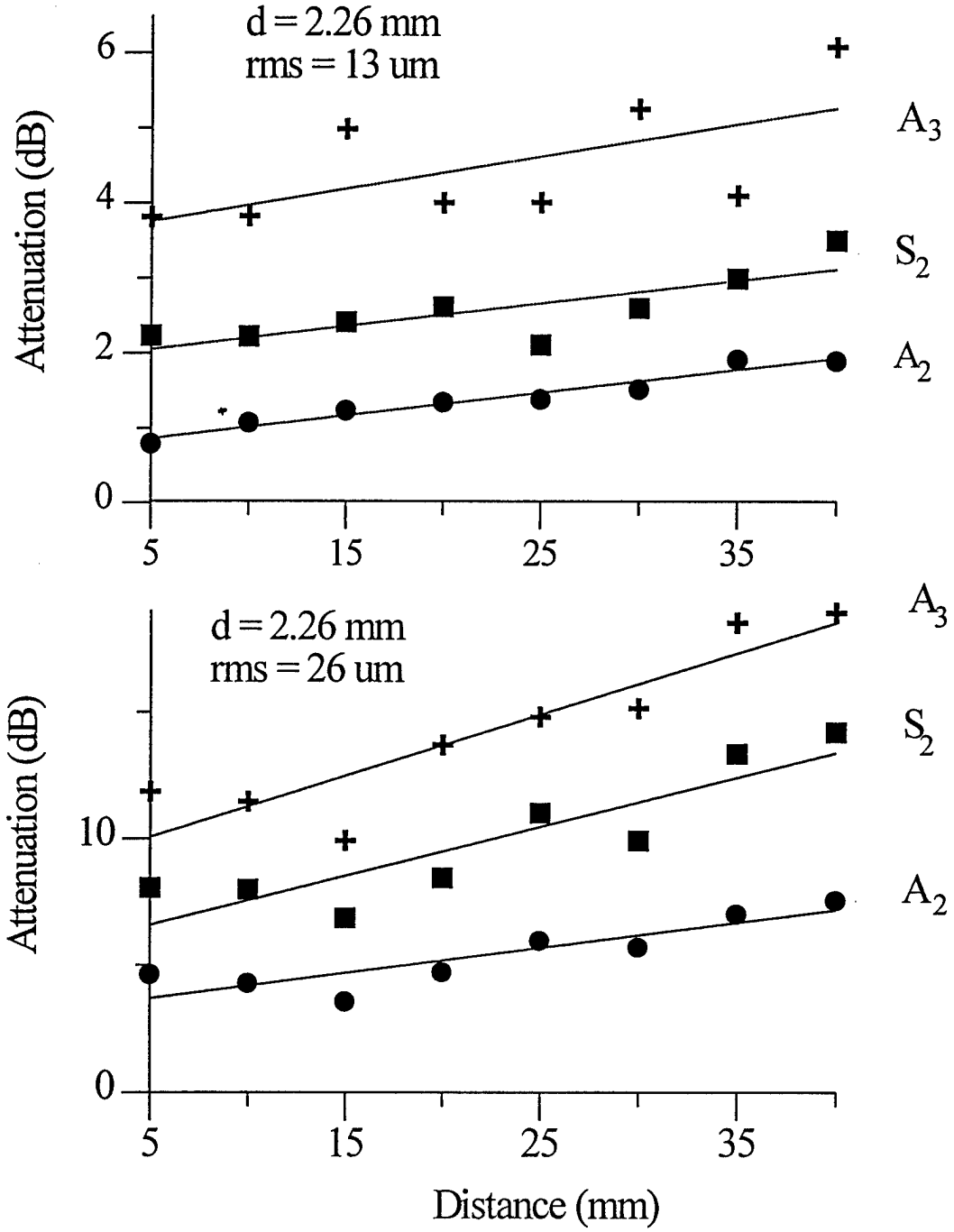

Figure 28: Collected experimental data for rough aluminum plates as a function of transducer axis separations x_i; three modes are illustrated for each of the two rms roughnesses, $h = 13$ μm and $h = 26$ μm.

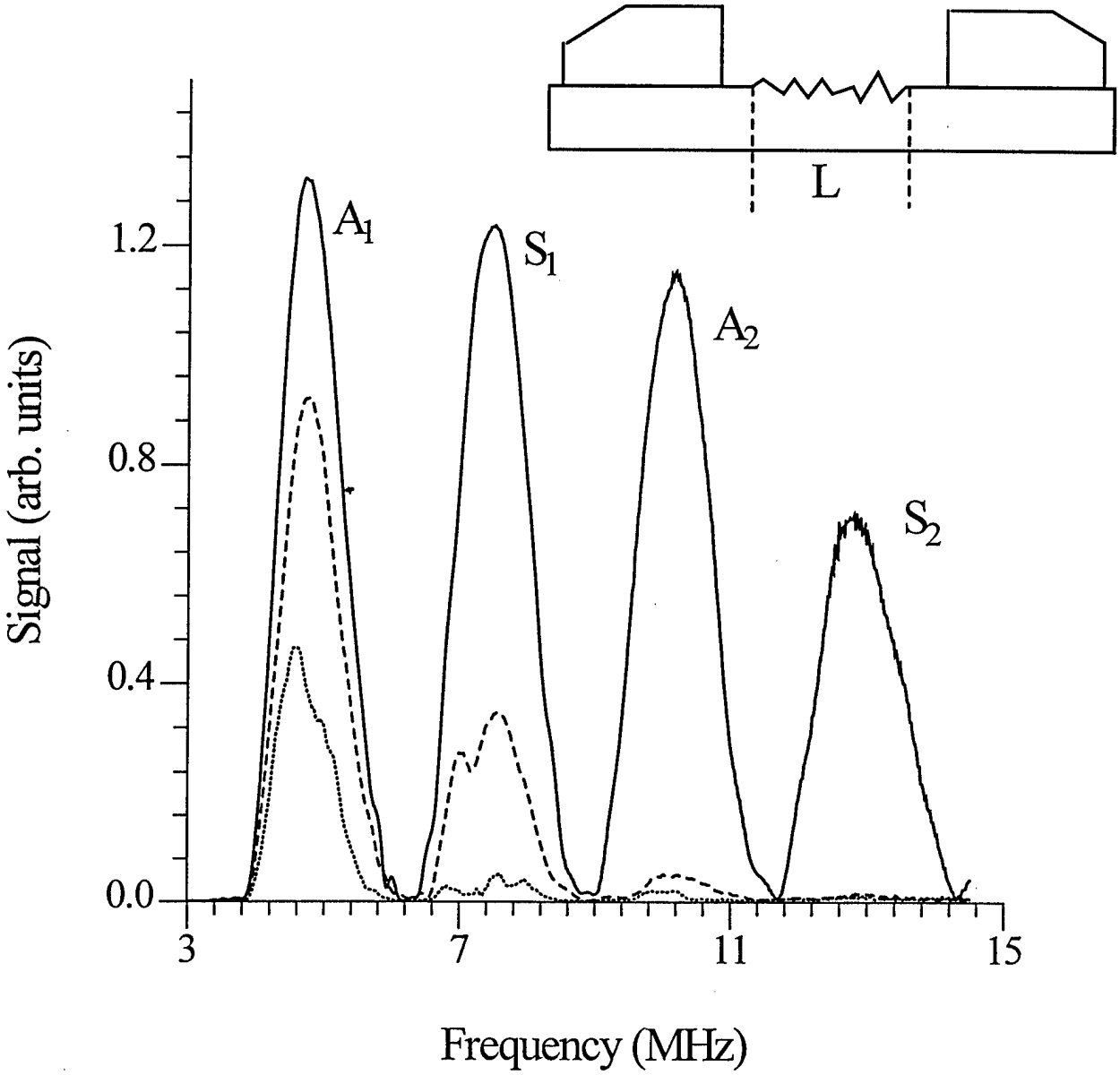

Figure 29: Shoe-contact experimental signal from rough aluminum plates ($h = 44$ μm) for two different roughness lengths L (solid: no roughness; dashed: 12.7 mm roughness section; dotted: 25.4 mm). Inset shows roughness on same side as transducers.

such a way that a ridge can develop between the roughened region and the smooth portion. This ridge can lead to decreased received signal owing to reflection at the interface. This effect is not modeled in our analysis, and so appears as a source of error. To show again that, for our purposes, these differences can be suppressed, we have analyzed these data and plotted the normalized peak amplitudes as a function of roughness length for the A_1 and S_1 modes in the indented plates. Here, we deal with discrete roughened sections, rather than the continuous roughness discussed above for Fig. 28. These data are shown in Fig. 32. Here, we also calculate the root slope ratio $\mathcal{R}_{S_1/A_1}$ for the two modes S_1 and A_1. In this case the root slope ratio should yield the frequency ratio of the two modes.

An improvement in the contact couplant technology should come from exploring the use of solid elastomer couplants.

4.3 Knife-Edge Contact Coupling

We have also explored, in a limited number of measurements, the character of data obtained using knife-edge type coupling wedges. These devices are also fabricated from polystyrene and are brought to a relatively narrow strip ($\sim$ 1 mm) that makes contact with the specimen. At this line contact, a broader range of spatial frequencies are generated than we obtain with conventional contact coupling, which would extend over 10 mm or more. The knife-edge is the spatial/wavenumber domain equivalent of a broadband transducer in the time/frequency domain. The knife-edge generates elastic energy at many wavenumbers. By contrast, the planar piston transducer we normally use has a fairly narrow directivity function, and generates an elastic farfield reasonably sharply peaked about the transducer central ray. Like the piston radiator, however, the knife-edge too will have a sharper directivity function as frequency increases.

Results for the knife-edge are shown in Fig. 33, where three curves are shown for a knife-edge contact separation of 22 mm. The solid curve is for a smooth surface, the dashed curve is 13-μm roughness, and the dotted curve is 26 μm. All curves have been normalized to remove both transducer frequency and polystyrene damping effects. With the knife-edge wedges we have found the expected behavior, namely that the sensitvity of the signal to contact force is much reduced. Therefore, contact problems are much less bothersome with knife-edge coupling than with conventional shoe-type contact wedges. Even with the relatively small roughness path of 22 mm, we find an interesting effect. The signals for the 26-μm roughness plate almost disappear in a frequency range from 3 to 8 MHz. The spatial bandwidth of the knife-edges decreases as the frequency approaches midband (4–8 MHz), and most of the acoustic energy is concentrated in a relatively narrow range about $\alpha = 0°$. This result makes sense for a contact width a of 1 mm, where the $k_p a$ at 5 MHz is about 5. For a very broad spatial radiator $k_p a$ should be less than 1.

But, the current choice of contact width may have an unforeseen advantage. The concentration of energy about $\alpha = 0°$ permits only the higher order modes near cutoff to

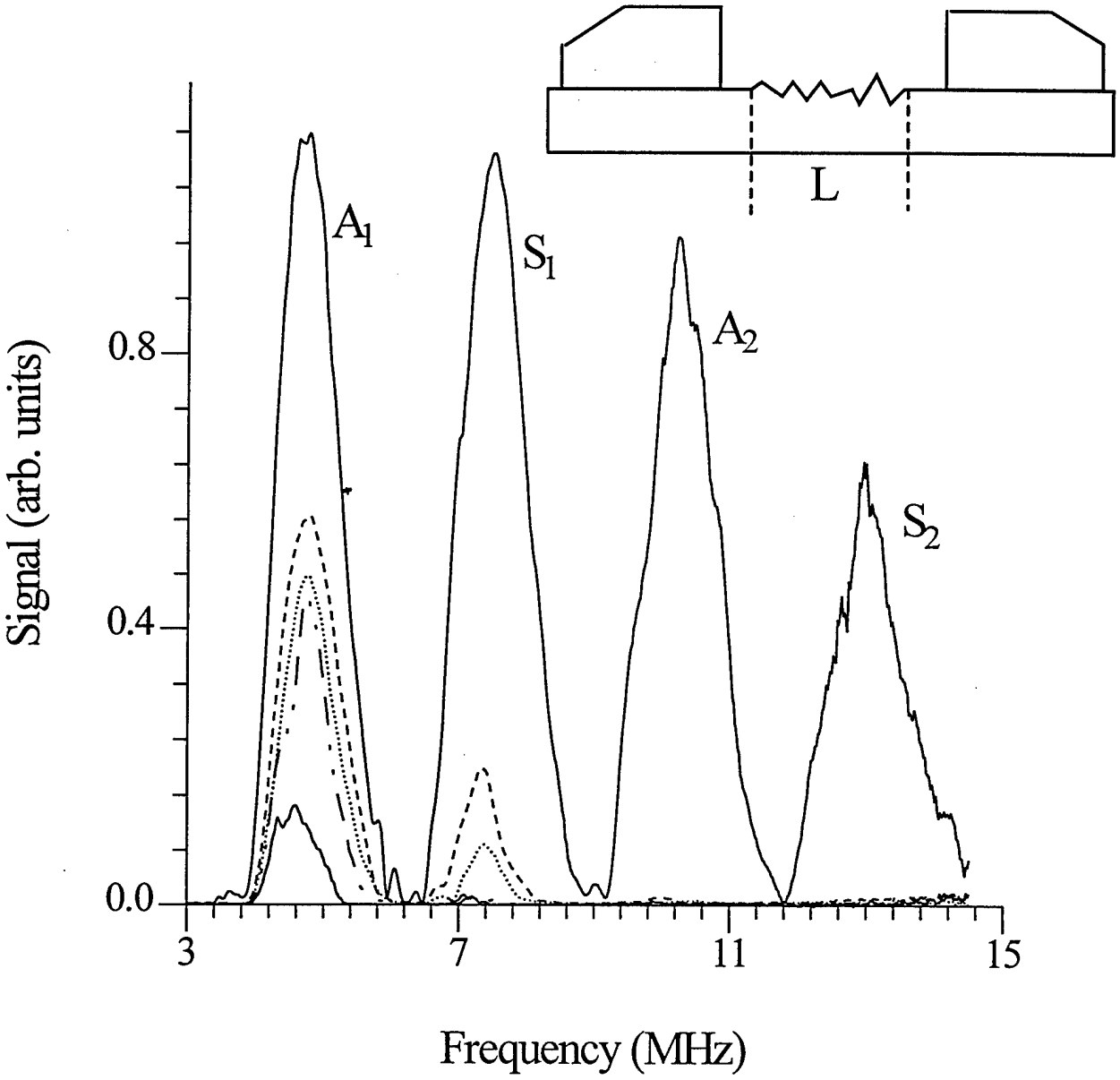

Figure 30: Shoe-contact experimental signal from rough aluminum plates ($h = 60$ μm) for four different roughness lengths L (solid: no roughness; dashed: 12.7 mm roughness section; dotted: 25.4 mm; chain dot: 38.1 mm; solid: 50.8 mm). Inset shows roughness on same side as transducers.

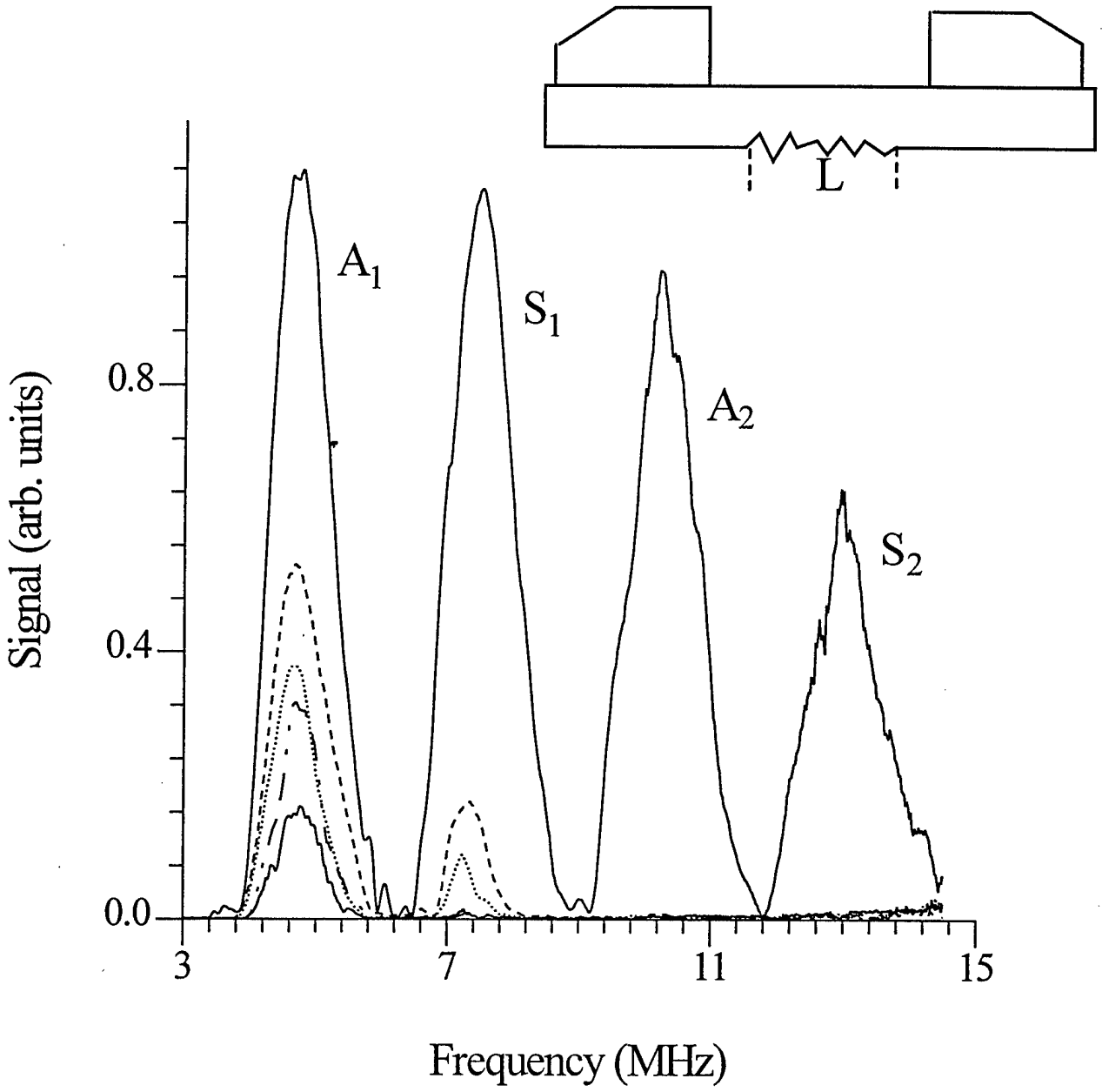

Figure 31: Shoe-contact experimental signal from rough aluminum plates ($h = 60$ μm) for four different roughness lengths L (solid: no roughness; dashed: 12.7 mm roughness section; dotted: 25.4 mm; chain dot: 38.1 mm; solid: 50.8 mm). Inset shows roughness on opposite side as transducers.

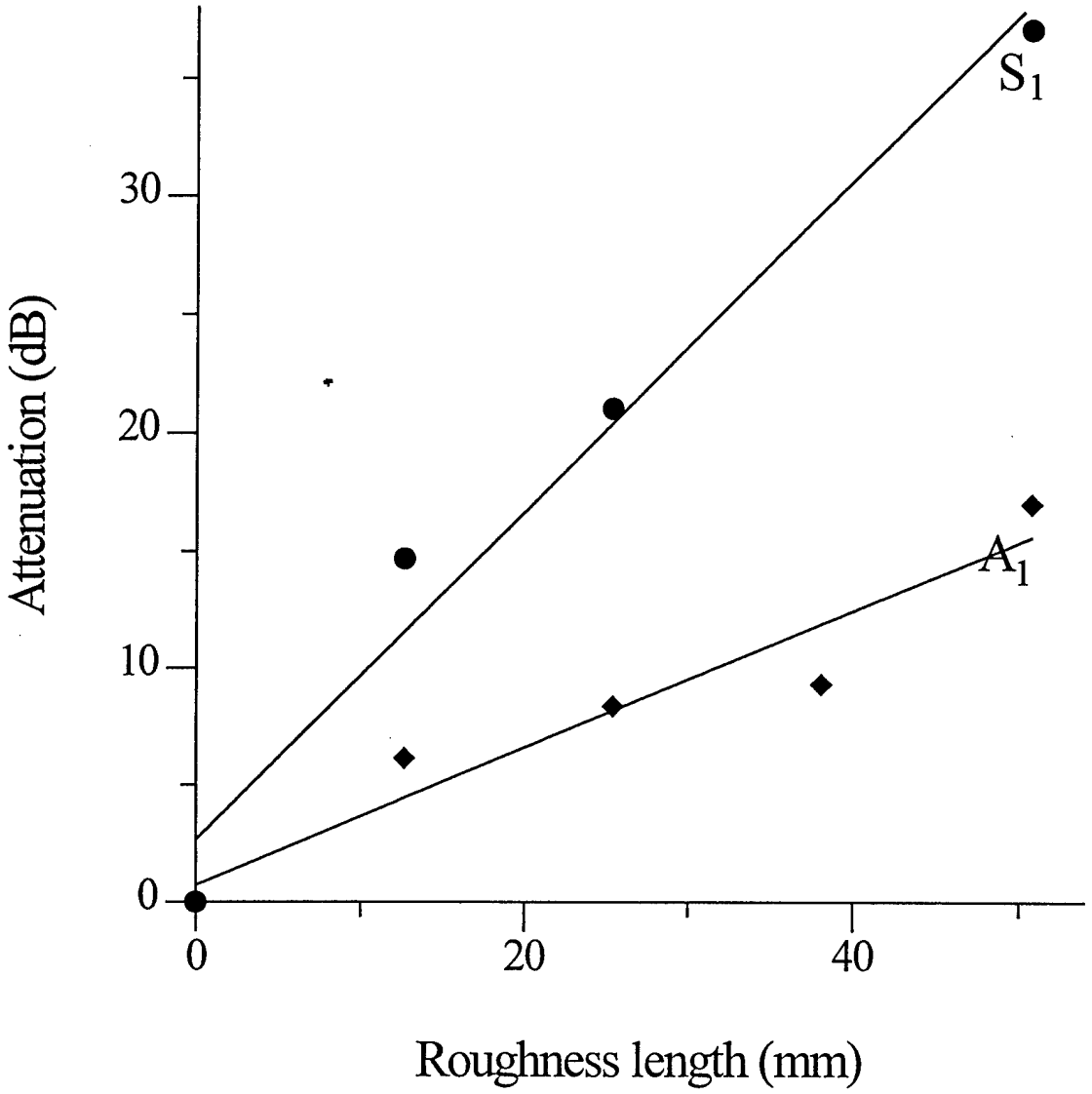

Figure 32: Collected experimental data for rough aluminum plates as a function of roughness section length L; two modes are illustrated for the 60-μm rms roughness plate, S_1 and A_1.

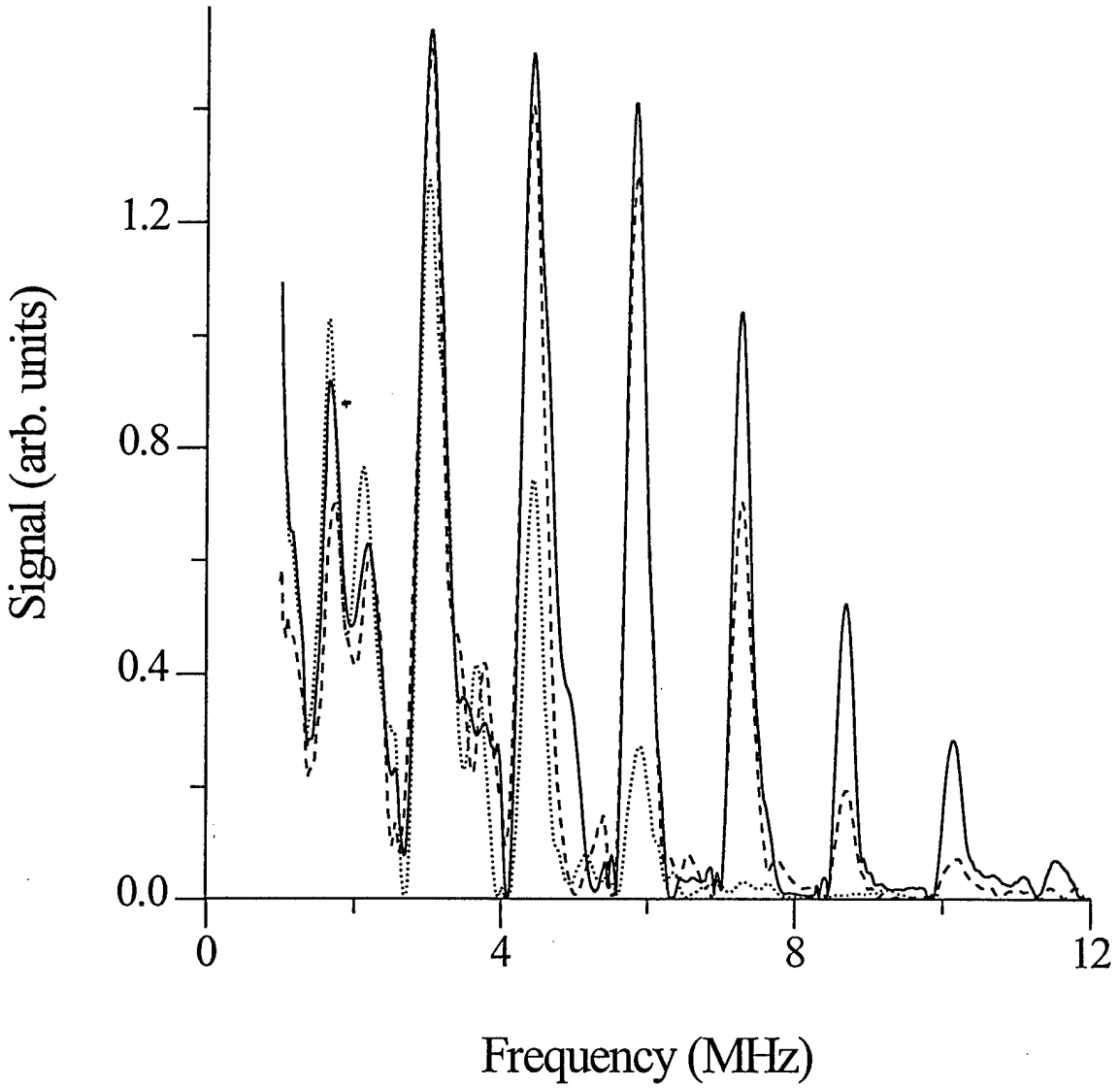

Figure 33: Knife-edge contact experimental signals from rough aluminum plates (dashed: $h = 13$ μm; dotted: $h = 26$ μm) for a transducer separation $x_i = 22$ mm. Sharp decrease in received signal from 26-μm RS between 3 and 8 MHz illustrates effect of narrowing spatial bandwidth.

be generated. From Fig. 1 this region (near mode cutoff) is most sensitive to roughness. When frequency and spatial bandwidth are suitably chosen, the signal contrast between smooth and rough surfaces should be strongly enhanced. This is exactly the circumstance with the 26-μm rough surface shown in Fig. 33 as the dotted curve. The dashed curve for 13-μm roughness in Fig. 33 only begins the steep drop (compared to the smooth surface) after 6 MHz. But because the angles near cutoff are favored, each peak in Fig. 33 will likely include contributions from one or more individual modes. From $\alpha = 0°$ to $\sim 10°$ ($V_{\text{phase}} = \infty$ to 12.7 km/s) the symmetric and antisymmetric modes are crossing each other and close approaches are possible. The magnitude of each mode's contribution to peaks in Fig. 33 depends on the strength of mode excitation, and this value is tied to the imaginary parts of the wavevector. While these results are somewhat preliminary, they clearly point towards a very fruitful line of work.

5 Summary and Recommendations

In this report we have examined the behavior of guided elastic waves in the presence of rough surfaces studied as a model of incipient corrosion. These investigations have led to a broader understanding of the phenomenology of rough surface interactions with elastic waves. Extensive measurements in immersion, contact mode, and with a knife edge demonstrate the wide range of physical behavior of elastic guided waves and their dependence on the condition of the guiding surfaces. These measurements have also led to a deeper understanding of challenges in finding optimal methods for the estimation of hidden surface roughness from ultrasonic guided wave measurements.

Moreover, we have developed a simple, easily calculated model of rough surface guided wave velocity dispersion showing all important features of the damping effects of rough guiding surfaces. The model incorporates the straightforward, yet powerful, phase-screen approximation by suitable modifications to the partial wave reflections at each guiding surface. The dispersion relation is derived using transverse resonance methods, while extension of these ideas to fluid-loaded plates is accomplished by applying a reflection series expression. This result isolates individual halfspace scattering coefficients, enabling us to treat one-sided roughness and roughness in the presence of fluid loading using the same partial wave approach.

Comparisons between predictions of the model and experimental data demonstrate rather good agreement across the entire parameter space we have investigated. This close agreement enhances confidence that a successful inversion algorithm can be developed from this technology. Not only in immersion testing where predictable wave conversion at interfaces occurs, but also for contact mode coupling, we have demonstrated that accurate quantitative results can be deduced from the data and these data agree remarkably well with the predictions of our model.

For the future, the work that remains to be done should concentrate on extensions of the current successful effort. In particular, these tasks should be pursued:

- Develop extended model for guided plate wave propagation in rough plates incorporating correlation length dependence;
- Conduct experiments on plates with rough surfaces to measure dispersion and attenuation using knife-edge coupling and deformable-solid contact;
- Develop theoretical model for scattering from crack-like defects in plates with rough surfaces;
- Measure rough surface-induced guided wave loss with solid couplant, knife-edge wedges, and in immersion to study the effects of the rough surface parameters on acquired experimental flaw signal;
- Investigate modeling and measurements in multilayer plates with roughness between and below layers;
- Utilize results to develop and test a practical inversion procedure which yields information on roughness characteristics, flaw location, and, possibly, flaw size.

References

[1] K. Buhler and A. F. Grandt, "Analysis of multiple-site damage with implications for nondestructive evaluation", in *Review of Progress in Quantitative NDE*, vol. 14B, eds. D. O. Thompson and D. E. Chimenti (Plenum, New York, 1995), 1947-1954.

[2] F. G. Bass and I. M. Fuks, *Wave Scattering from Statistically Rough Surfaces*, (Pergamon Press, Oxford, 1979).

[3] D. K. Dacol and D. H. Berman, "Sound scattering from a randomly rough fluid-solid interface", J. Acoust. Soc. Am. **84**, 292-302 (1988).

[4] D. H. Berman, "Effective reflection coefficients for the mean acoustic field between two rough interfaces", J. Acoust. Soc. Am. **96**, 417-26 (1994).

[5] F. M. Labianca and E. Y. Harper, "Connection between various small waveheight solutions of the problem of scattering from the ocean surface", J. Acoust. Soc. Am. **62**, 1144-57 (1977).

[6] W. A. Kuperman and H. Schmidt, "Self-consistent perturbation approach to rough surface scattering in stratified elastic media", J. Acoust. Soc. Am. **86**, 1511-22 (1995).

[7] H. Schmidt, and W. A. Kuperman, "Spectral representations of rough interface reverberation in stratified ocean waveguides", J. Acoust. Soc. Am. **97**, 2199-209 (1995).

[8] J. T. Fokkema, "Reflection and transmission of elastic waves by the spatially periodic interface between two solids (numerical results for the sinusoidal interface)", Wave Motion **3**, 33-48 (1981).

[9] A. Lakhtakia, V. K. Varadan, and V. V. Varadan, "Scalar scattering characteristics of a periodic, impenetrable surface: effect of surface modeling errors", J. Appl. Phys. **60**, 4090-4 (1986).

[10] A. El-Bahrawy, "Guided modes in a layered elastic half-space with doubly corrugated surfaces", J. Acoust. Soc. Am. **96**, 3155-66 (1994).

[11] J. D. Sheard and M. Spivak, "Wave scattering in a rough elastic layer adjoining a fluid halfspace", J. Acoust. Soc. Am. **97**, 72-83 (1995).

[12] C. Eckhart, "The scattering of sound from the sea surface", J. Acoust. Soc. Am. **25**, 566-70 (1953).

[13] J. A. Ogilvy, Nondestruct. Test. **19**, 371 (1986).

[14] P. B. Nagy and L. Adler, "Surface roughness induced attenuation of reflected and transmitted ultrasonic waves", J. Acoust. Soc. Am. **82**, 193-197, 1987.

[15] P. B. Nagy and J. H. Rose, "Surface roughness and the ultrasonic detection of subsurface scatterers", J. App. Phys. **73**, 566-580, 1993.

[16] J. A. Ogilvy, *Theory of wave scattering from random rough surface*, (Adam Hilger, London, 1991).

[17] D. K. Dacol, "The Kirchhoff approximation for acoustic scattering from a rough fluid-elastic solid interface", J. Acoust. Soc. Am. **88**, 978-83 (1990).

[18] P. P. Goswami, T. J. Rudolphi, F. J. Rizzo, and D. J. Shippy, "A boundary element method for acoustic-elastic interaction with applications in ultrasonic NDE", J. Nondestructive Evaluation **9**, 101-112 (1990).

[19] J. H. Rose, M. Bilgen and P. B. Nagy, "Acoustic double-reflection and transmission at a rough water-solid interface", J. Acoust. Soc. Am. **95**, 3242-3251 (1994).

[20] M. DeBilly and G. Quentin, "Backscattering of acoustic waves by randomly rough surfaces of elastic solids immersed in water", J. Acoust. Soc. Am. **72**(2), 591-601 (1982).

[21] S. L. Broschat, E. I. Thorsos, and A. Ishimaru, "The phase perturbation technique vs. an exact numerical method for random rough surface scattering", J. Electromag. Waves Appl. **3**(3), 237-256 (1989).

[22] E. I. Thorsos, "The validity of the Kirchhoff approximation for rough surface scattering using Gaussian roughness spectrum", J. Acoust. Soc. Am. **83**, 78-92 (1988).

[23] E. I. Thorsos, "The validity of the perturbation approximation for rough surface scattering using a Gaussian roughness spectrum", J. Acoust. Soc. Am. **86**, 261-277 (1989).

[24] Y. A. Kravtsov and A. I. Saichev, "Effects of double passage of waves in randomly inhomogeneous media", Sov. Phys. Usp. **25**, 494-508 (1982).

[25] E. Jakeman, "Enhanced backscattering through a deep random phase screen", J. Opt. Soc. Am. **A 5**, 1638-1648 (1988).

[26] B. A. Auld, *Acoustic Waves and Fields in Solids*, 2nd ed, (Krieger, Malabar, FL, 1990).

[27] O. I. Lobkis, A. Safaeinili, and D. E. Chimenti, "Precision ultrasonic reflection studies in fluid-coupled plates", J. Acoust. Soc. Am. **99**, 2727-36 (1996).

[28] L. B. Felsen and N. Marcuvitz, *Radiation and Scattering of Waves*, (Prentice-Hall, Englewood Cliffs, NJ, 1973).

[29] L. M. Brekhovskikh and O. A. Godin, *Acoustics of Layered Media II*, (Springer-Verlag, Berlin, 1992), Chap. 5.

[30] A. Safaeinili and R. A. Roberts, "An efficient approximate model for elastic wave scattering in plates", in *Review of Progress in Quantitative NDE*, vol. 14A, eds. D. O. Thompson and D. E. Chimenti (Plenum, New York, 1995), 147-154.

[31] A. Safaeinili, O. I. Lobkis, and D. E. Chimenti, "Air-coupled ultrasonic characterization of composite plates", Materials Eval. 53, 1186-90 (1995).

[32] A. Safaeinili, O. I. Lobkis, and D. E. Chimenti, "Air-coupled ultrasonic estimation of viscoelastic stiffnesses in plates", IEEE Trans. UFFC, accepted for publication.

[33] B. Drinkwater and P. Cawley, "The effect of dust and surface roughness on the efficiency of solid-coupled wheel probes", in *Review of Progress in Quantitative NDE*, vol. 15A, eds. D. O. Thompson and D. E. Chimenti (Plenum, New York, 1996), 955-62.

[34] D. E. Chimenti and A. H. Nayfeh, "Ultrasonic reflection and guided wave propagation in biaxially laminated composite plates", J. Acoust. Soc. Am. 87, 1409-1415 (1990).

[35] M. Deschamps and C.-W. Cao, Reflection /refraction of a solid layer by Debye's series expansion, Ultrasonics 29, 288-96 (1991).